3D Wave Propagation Simulations of M_w 6.5+ Earthquakes on the Tacoma Fault, Washington State, Considering the Effects of Topography, a Geotechnical Gradient, and a Fault Damage Zone

Ian Stone*[1], Erin A. Wirth[1], Alex Grant[1], and Arthur D. Frankel[1]

ABSTRACT

We simulate shaking in Tacoma, Washington, and surrounding areas from M_w 6.5 and 7.0 earthquakes on the Tacoma fault. Ground motions are directly modeled up to 2.5 Hz using kinematic, finite-fault sources; a 3D seismic velocity model considering regional geology; and a model mesh with 30 m sampling at the ground surface. In addition, we explore how adjustments to the seismic velocity model affect predicted shaking over a range of periods. These adjustments include the addition of a region-specific geotechnical gradient, surface topography, and a fault damage zone. We find that the simulated shaking tends to be near estimates from empirical ground-motion models (GMMs). However, long-period (T = 5.0 s) shaking within the Tacoma basin is typically underpredicted by the GMMs. The fit between simulated and GMM-derived short-period (T = 0.5 s) shaking is significantly improved with the addition of the geotechnical gradient. From comparing different M_w 6.5 earthquake scenarios, we also find that the response of the Tacoma basin is sensitive to the azimuth of incoming seismic waves. In adding surface topography to the simulation, we find that average ground motion is similar to that produced from the nontopography model. However, shaking is often amplified at topographic highs and deamplified at topographic lows, and the wavefield undergoes extensive scattering. Adding a fault damage zone has the effect of amplifying short-period shaking adjacent to the fault, while reducing far-field shaking. Intermediate-period shaking is amplified within the Tacoma basin, likely due to enhanced surface-wave generation attributable to the fault damage zone waveguide. When applied in the same model, the topography and fault damage zone adjustments often enhance or reduce the effects of one another, adding further complexity to the wavefield. These results emphasize the importance of improving near-surface velocity model resolution as waveform simulations progress toward higher frequencies.

KEY POINTS

- Despite being able to simulate high-frequency (HF) shaking, modern simulations still struggle with accuracy.
- By making targeted updates to a standard velocity model, we improve HF shaking estimates relative to GMMs.
- Further improvement of direct earthquake simulation is tied to site- and region-specific characterization.

Supplemental Material

INTRODUCTION

Direct simulation of earthquake shaking has become a common component of urban seismic hazard analysis. The method provides a means to model ground motion with consideration towards the sort of source complexity and 3D path effects that traditional ground-motion models (GMMs) struggle to constrain. By simulating a suite of scenarios spanning likely rupture parameters, one can capture the range of possible ground motions from a given fault while also illuminating the factors that most influence the ground-motion

1. U.S. Geological Survey, Earthquake Science Center, Seattle, Washington, U.S.A., https://orcid.org/0000-0003-2622-2691 (IS); https://orcid.org/0000-0002-8592-4442 (EAW); https://orcid.org/0000-0002-5096-4305 (AG); https://orcid.org/0000-0001-9119-6106 (ADF)

*Corresponding author: istoneuw@gmail.com

Cite this article as Stone, I., E. A. Wirth, A. Grant, and A. D. Frankel (2023). 3D Wave Propagation Simulations of M_w 6.5+ Earthquakes on the Tacoma Fault, Washington State, Considering the Effects of Topography, a Geotechnical Gradient, and a Fault Damage Zone, *Bull. Seismol. Soc. Am.* **113**, 2519–2542, doi: 10.1785/0120230083

© Seismological Society of America

Downloaded from http://pubs.geoscienceworld.org/ssa/bssa/article-pdf/113/6/2519/6037178/bssa-2023083.1.pdf
by University of Washington user

variability. The method is particularly useful in areas with inherently high seismic hazard but low background seismicity, like Washington State's Puget Sound region. In this region, previous simulations have been used to constrain the likely ground motions from both the interplate megathrust earthquakes on the Cascadia subduction zone (Frankel *et al.*, 2018; Wirth, Frankel, *et al.*, 2018), as well as large earthquakes on crustal faults (Frankel *et al.*, 2007, 2009; Allstadt *et al.*, 2013; Stone *et al.*, 2022). These simulations have been the basis for much of the region's urban seismic hazard planning over the last decade (e.g., Frankel *et al.*, 2007; Wirth, Chang, and Frankel, 2018).

In this study, we seek to build on this past work by conducting simulations of earthquakes on the Tacoma fault. The previous simulations of crustal earthquakes in the Puget Sound have focused primarily on the Seattle fault and, to a lesser extent, the southern Whidbey Island fault (Frankel *et al.*, 2007; Allstadt *et al.*, 2013; Stone *et al.*, 2022). In contrast, there has been very little work to simulate earthquakes on the Tacoma fault, even though it has a similar estimated recurrence rate and maximum magnitude, while threatening much of the same region. We seek to establish a baseline set of ground-shaking scenarios in the south Puget Sound region from M_w 6.5+ earthquakes on the Tacoma fault. These scenarios incorporate a nonplanar source model and span a variety of different source configurations, including 18 combinations of different slip distributions and hypocenter locations. Modeled ground motions are 100% physics-based (i.e., without a stochastic amendment) and have a maximum frequency of approximately 2.5 Hz.

In addition, we seek to compare shaking between different versions of the regional 3D seismic velocity model adjusted to consider factors that affect higher frequency (>1 Hz) shaking. Direct earthquake simulations now routinely exceed 1 Hz in their maximum modeled frequency (e.g., Rodgers *et al.*, 2020; Castro-Cruz *et al.*, 2022; Hu *et al.*, 2022; Stone *et al.*, 2022). However, the velocity models used in most simulations do not have the level of detail needed to accurately reproduce high-frequency shaking. Factors like surface topography (Stone *et al.*, 2022) and near-fault velocity heterogeneity (Graves and Pitarka, 2016), as well as shallow velocity structure and soil nonlinearity (Frankel *et al.*, 2002), can all impact the strength and variability of high-frequency shaking. Because they could not be constrained at the level of detail necessary for accurate simulation, or because simulations could not directly incorporate them, these factors have often been handled reductively in postprocessing, or simply not considered at all. The ability to simulate ground motions at much higher frequencies provides an opportunity to re-evaluate and adjust existing velocity models for use in the next generation of earthquake simulations. With this in mind, we make three adjustments to the U.S. Geological Survey's (USGS) Cascadia Velocity Model (CVM; Stephenson *et al.*, 2017): we add a region-specific geotechnical gradient, surface topography, and a low-velocity fault damage zone. These factors are known to influence shaking above 1 Hz, and with a fine-scale model mesh (i.e., <100 m discretization at the surface) and sufficient computing power, they can be explicitly included in regional-scale simulations. We investigate how these factors influence shaking relative to the original velocity model as well as how their effects interact with one another to impact ground motions.

Regional geology and the Tacoma fault

The Tacoma fault is one of the several east–west-trending crustal faults that cross the Puget Lowland—a large, partially submerged forearc basin situated between the Olympic and Cascade mountain ranges in Washington State. Since ~40 Ma, the Tacoma fault, along with the Seattle and southern Whidbey Island faults, have accommodated tens of kilometers of north–south shortening in the region (Johnson *et al.*, 1994, 1999; Pratt *et al.*, 1997). The faults bound several asymmetric sedimentary basins (from north to south, the Everett, Seattle, and Tacoma basins), each of which are several kilometers deep (Brocher *et al.*, 2001). Despite the significant offset along these faults, the surface expression of faulting is relatively subtle, particularly in the central portion of the Puget Sound region. This is partially a result of glaciation, which reworked the regional topography during past ice ages, while depositing a thick layer of glacial till on the surface. The unique geology of the area lends itself to enhanced earthquake shaking. In particular, the Seattle basin has demonstrated a propensity toward intermediate- and long-period amplification during historic earthquakes, with shaking at 1 Hz more than doubled inside the basin relative to sites outside the basin (Frankel *et al.*, 2002). An abundance of areas underlain by shallow soft soils (e.g., river sediments, lahar deposits, and artificial fill) also encourages widespread shaking amplification and liquefaction during large earthquakes (Frankel *et al.*, 1999, 2002; Hartzell *et al.*, 2000; Rekoske *et al.*, 2021). Similarities in geology suggest that the Tacoma and Everett basins may also amplify earthquake shaking, but only a few direct earthquake shaking observations exist in these basins (Thompson *et al.*, 2020; Rekoske *et al.*, 2021).

The Tacoma fault has been mapped through a combination of seismic, potential field, and surface rupture measurements, and stretches at least 60 km across the south-central Puget Sound. The feature delineates the boundary between the Tacoma basin to the south and the Seattle uplift to the north. Geophysical studies on the fault either have it dipping at a steeper 60° (Brocher *et al.*, 2001) or a shallower 45° (Brocher *et al.*, 2004; Johnson *et al.*, 2004) to the north, depending on the method used. For this study, we adopt the shallower dipping model, because it is determined from a broader range of methods. The fault accommodates reverse or reverse-oblique slip (Brocher *et al.*, 2001, 2004; Johnson *et al.*, 2004).

The last paleoseismically recorded event occurred on the fault ~1100 yr B.P., with a modeled magnitude around M_w 7 (Bucknam *et al.*, 1992; Sherrod *et al.*, 2002). Based on

Downloaded from http://pubs.geoscienceworld.org/ssa/bssa/article-pdf/113/6/2519/6037178/bssa-2023083.1.pdf
by University of Washington user

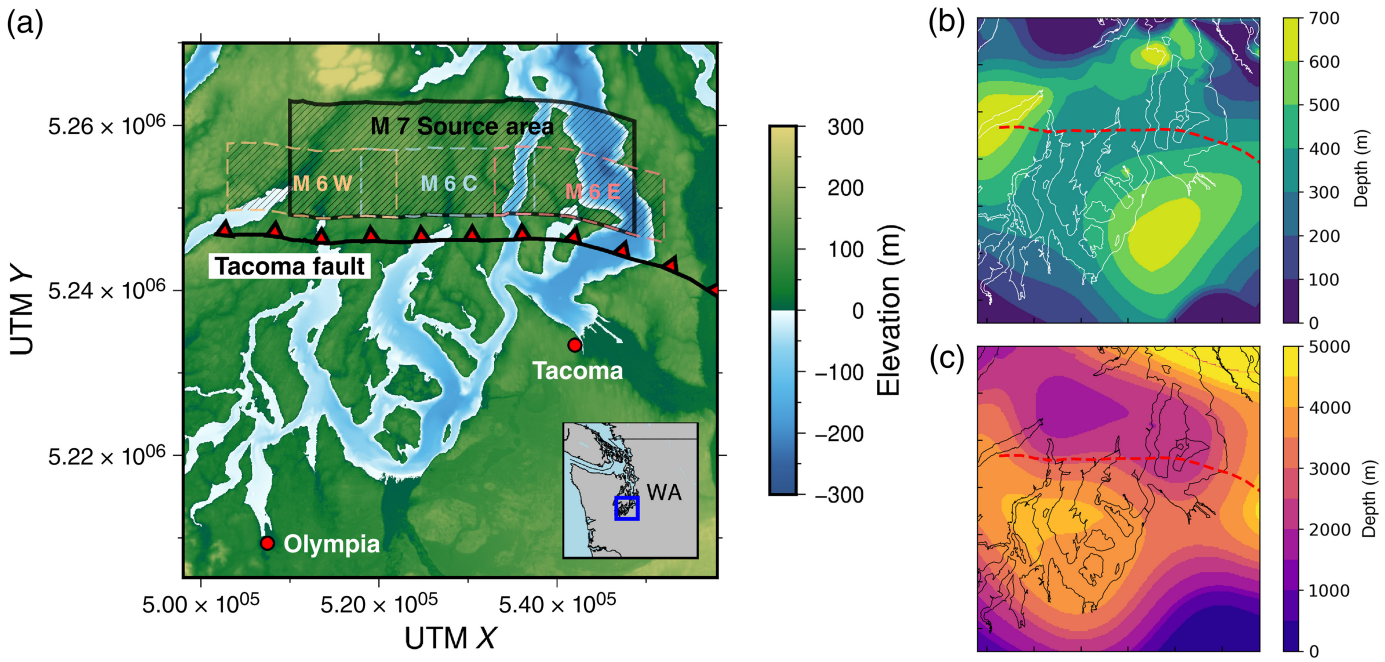

Figure 1. Model region and source areas. (a) Map of the model area, including 30 m sampled topography and bathymetry. The shaded areas denote the surface projections of the M_w 7.0 and 6.5 source planes (M 6 W/C/E = M_w 6.5 west/central/east source locations). The inset shows the location of the study area within Washington State. (b) Depth to the base of Quaternary sedimentary materials (i.e., V_S = 1000 m/s). (c) Depth to the base of Tertiary sedimentary materials (i.e., V_S = 2500 m/s). The color version of this figure is available only in the electronic edition.

geologic inferences from seismic imaging, it is estimated that the fault accommodates at least 0.2 mm/yr of shortening, which would allow it to host M_w 6.5+ events every few thousand years (Johnson *et al.*, 2004). Some studies argue that the Tacoma fault is a large-scale backthrust of the south-dipping Seattle fault, suggesting that the faults intersect at depth and may have dependent slip behavior (Brocher *et al.*, 2004; Johnson *et al.*, 2004). Surface ruptures of the fault have been mapped along its western extent on the Kitsap peninsula (Sherrod *et al.*, 2004); surface expressions of the fault are not apparent on the east side of the Puget Sound; and the surface trace has largely been constrained via active seismic and potential-field surveys (Johnson *et al.*, 2004). A modern-day earthquake on the fault would threaten the cities of Tacoma, Olympia, and Seattle, as well as nearby ports, airports, and military infrastructure.

METHOD

Source model

The kinematic source model used in this study was based on the method applied by Frankel *et al.* (2014) and is largely the same as the model applied by Stone *et al.* (2022). The slip pattern was initially defined using a randomly seeded fractal distribution. Spectral amplitudes of this distribution are flat up to a characteristic wavenumber (k), before decaying at a rate of k^{-2} above that value. The correlation distances in the along-strike and down-dip directions, defined using the magnitude dependency relation of Mai and Beroza (2002), were set to 14.6 and 6.9 km for the M_w 7.0 source, and 8.0 and 4.6 km for the M_w 6.5 source. Slip was linearly tapered to zero at the edges of the distribution using a 3 km buffer zone.

The slip distribution was discretized into a grid of subsources spaced at 0.5 km. The slip velocity across the source distribution assumed an average value of 1.0 m/s and was randomly perturbed by ±20%, consistent with the empirical observations of Somerville *et al.* (1999). Rise times were then calculated by dividing the slip at each subsource by the local slip velocity.

To determine rupture initiation times, we set the average rupture velocity across the source to 80% of the local S-wave velocity. This value was allowed to vary based on the amount of slip at each subsource, such that areas with greater slip had faster rupture velocities, and areas with lower slip had slower rupture velocities. Rupture initiation times were then calculated using 2D ray tracing. The slip fashion for each subsource was described using a moment tensor representing reverse slip, and the source time function was described using a Brune pulse (Brune, 1970).

We modeled the Tacoma fault along the primary northern surface trace from the U.S. Geological Survey Quaternary Fault Database (Brocher *et al.*, 2016), as shown in Figure 1. We assumed a fault dip of 45° to the north, consistent with the findings of Brocher *et al.* (2004) and Johnson *et al.* (2004). The along-strike location of each subsource was determined based on distance along the fault trace. The down-dip location of the subsources was determined by projecting the fault trace linearly down-dip. Source dimensions were determined using

Downloaded from http://pubs.geoscienceworld.org/ssa/bssa/article-pdf/113/6/2519/6037178/bssa-2023083.1.pdf
by University of Washington user

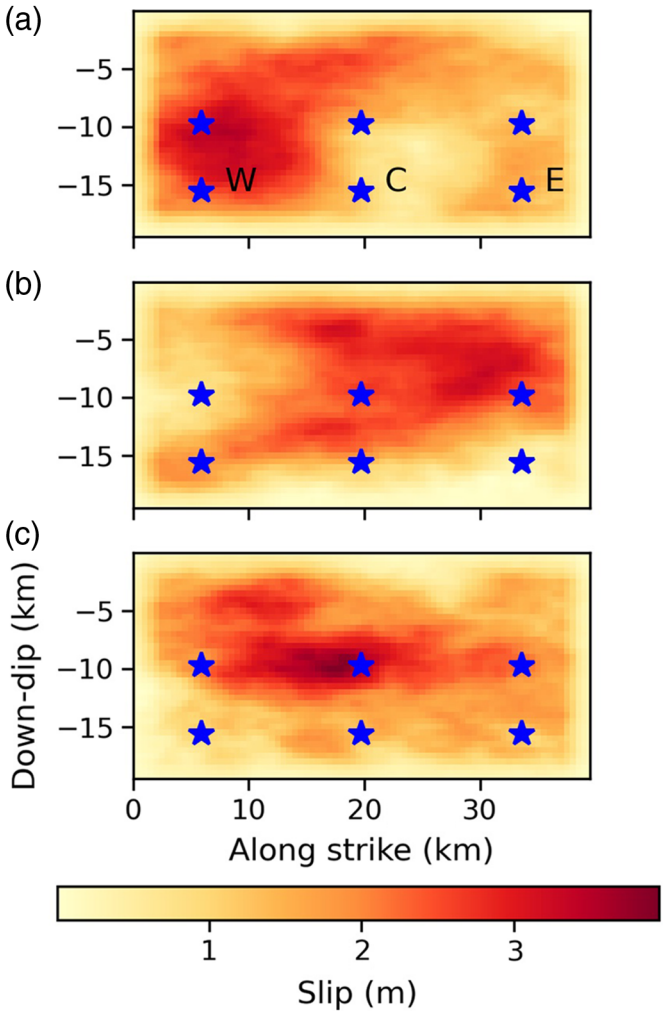

Figure 2. Slip distributions and hypocenter locations for the 18 M_w 7.0 source realizations. (a–c) Distributions describing the amount of slip on the fault surface. The stars denote the six different hypocenter locations (C, central; E, east; and W, west). The upper row of stars corresponds to the "mid" hypocenters, and the lower row of stars corresponds to the "deep" hypocenters. The color version of this figure is available only in the electronic edition.

the relations of Wells and Coppersmith (1994). The M_w 7.0 sources were 40 km along-strike and 20 km down-dip; and the M_w 6.5 sources were 20 km along-strike and 12 km down-dip. For all rupture scenarios, the top of the rupture was at a depth of 3 km.

To constrain a more complete set of likely ground motions from a Tacoma fault earthquake, we ran multiple M_w 6.5 and 7.0 scenarios in which we varied kinematic rupture parameters. Making up these permutations were three different hypocenter locations (west, central, and east), two hypocenter depths (50% and 80% of the way down-dip on the fault plane), and three different slip distributions (Fig. 2). In addition, we ran a subset of tests in which the M_w 6.5 source was shifted either to the west or east relative to its primary central location (Fig. 1). All the permutations discussed in this article are listed in Table 1. Each simulation was computed out to 60 s after rupture initiation.

Mesh

We directly simulated Tacoma fault earthquakes via spectral element method modeling. Simulations were run using the code SPECFEM3D, which was chosen for its efficiency in parallel computing settings and its handling of fine-scale, near-surface structure, including topography (Komatitsch *et al.*, 2004). We discretized the model space into a mesh composed of variably sized hexahedra. Mesh elements reduced in dimension approaching the ground surface by factors of 3, such that mesh elements deeper than 1200 m had an average size of 300 m, elements between 1200 and 300 m depth had an average size of 100 m, and elements shallower than 300 m had a size of ~33 m. The reduction in element size supports modeling of higher frequency shaking near the surface, where the velocities were much lower than at depth, as well as to reasonably accommodate surface topography. Surface topography was taken from the National Aeronautics and Space Administration (NASA) Shuttle Radar Topography Mission dataset sampled at an interval of 30 m (National Aeronautics and Space

TABLE 1
Descriptions of the 153 Primary Simulations Run for This Study

Sources	Velocity Model	Number of Slip Distributions	Number of Hypocenter Locations	Number of Hypocenter Depths (M_w 7.0/6.5)	Number of Simulations
M_w 7.0	CVM	3	3	2/0	**18**
M_w 7.0 and 6.5	CVM + GG	3	3	2/2	**36**
M_w 7.0 and 6.5	CVM + GG + T	3	3	2/1	**27**
M_w 7.0 and 6.5	CVM + GG + FDZ	3	3	2/1	**27**
M_w 7.0 and 6.5	CVM + GG + T + FDZ	3	3	2/1	**27**
M_w 6.5 west	CVM + GG	3	3	1	**9**
M_w 6.5 east	CVM + GG	3	3	1	**9**
				Total number of simulations	**153**

Unless otherwise specified, M_w 6.5 sources used the central source location. The bold entries describe the total number of each type of simulation. CVM, Cascadia velocity model; FDZ, fault damage zone; GG, geotechnical gradient; and T, topography.

Downloaded from http://pubs.geoscienceworld.org/ssa/bssa/article-pdf/113/6/2519/6037178/bssa-2023083.1.pdf
by University of Washington user

Administration [NASA] Shuttle Radar Topography Mission [SRTM], 2013); we combined this dataset, which only has elevations above sea level, with regional bathymetry from the National Oceanic and Atmospheric Administration (NOAA) (National Oceanic and Atmospheric Administration [NOAA] National Centers for Environmental Information, 2014). To improve mesh stability, a smoothed version of the topographic surface was used to define the refinement boundary at 300 m depth (i.e., the depth at which average element dimension decreases from ~100 to 30 m). Versions of the simulation that did not explicitly consider topography were run on a mesh with a flat free surface applying the same element dimension scheme as described earlier. Each simulation was run on the USGS' Denali Supercomputer (Falgout *et al.*, 2019), typically requiring 16 nodes (640 central processing units) and taking ~48 hr to complete.

CVM

All simulations employed the 3D seismic velocity model of Stephenson *et al.* (2017) (i.e., the CVM). Starting with a framework based on the primary regional geologic regimes, the CVM incorporates large-scale seismic variation using results from seismic tomography studies (Moschetti *et al.*, 2007) as well as some finer-scale variability in the Puget Sound region (e.g., Ramachandran *et al.*, 2006). Notably, the model directly represents the extensive Quaternary and Tertiary sediment layers present within the Puget Sound region, which allows for accurate simulation of basin effects. The model has been validated in simulations of observed earthquakes (Frankel *et al.*, 2009; Thompson *et al.*, 2020), and applied in a variety of regional- and local-scale ground-motion simulations (Frankel *et al.*, 2018; Wirth, Frankel, *et al.*, 2018; Wirth *et al.*, 2019; Stone *et al.*, 2022).

The current CVM is limited with respect to near-surface detail (i.e., <100 m depth) due to the resolution of its input datasets. As a result, the model has a comparatively high-minimum V_S relative to soils found in many parts of the region, and modeled ground motions are less sensitive to features that can influence shaking above 1 Hz (e.g., topography). For our simulations, we made two primary near-surface updates to the CVM: we added a shallow (<~100 m depth) geotechnical gradient; and we added surface topography. We additionally implemented and tested the influence of a near-fault damage zone.

A new compilation of over 900 velocity profiles in the Pacific northwest (Ahdi *et al.*, 2017) has allowed for modeling of regionally appropriate soil velocity models that can capture near-surface site response for velocities down to 100 m/s. To add a geotechnical gradient to the CVM, we refit the generalized equations for depth-dependent shear-wave velocity as a function of V_{S30} (Wirth *et al.*, 2021) for velocity profiles measured within the Puget Lowland in the Ahdi *et al.* (2017) compilation. Using 267 V_S measurements in the Puget lowland, V_S as a function of V_{S30} and depth (z) was computed as follows:

$$V_S(z,V_{S30}) = V_{S0} + Az + B\ln(z), \tag{1}$$

$$V_{S0} = -7.898 + 0.498V_{S30}, \tag{2a}$$

$$A = 1.733 + 0.013V_{S30}, \tag{2b}$$

$$B = -53.402 + 0.231V_{S30}, \tag{2c}$$

in which V_{S0} is the shear-wave velocity at the ground surface. A, B, and V_{S0} (equations 2a–2c) are model-fitting parameters derived from predictions on overlapping 20 m/s bins of V_{S30} from 100 to 900 m/s.

For each site, new V_S values were assigned in the upper portions of the CVM based on equation (1), until the depth was reached in which V_S from equation (1) exceeded the V_S value assigned at that depth in the CVM. This typically occurred at 100–200 m depth and, thus, represents the thickness of the geotechnical gradient. At deeper depths, V_S values from the original CVM are retained. An example profile comparing the original and amended CVM is included in Figures S1 and S2, available in the supplemental material to this article.

The V_{S30} values used to adjust the relations to individual sites were taken from the USGS topographic-slope-based V_{S30} atlas (Heath *et al.*, 2020). This atlas does not consider bathymetry and, thus, applies a constant V_{S30} value of 300 m/s in areas covered by water. To adjust for this, we calculated V_{S30} values using regional bathymetry and the method outlined in Wald and Allen (2007). The offshore V_{S30} values were replaced with the resulting estimates.

Topography was added to the CVM in much the same manner as in Stone *et al.* (2022). The primary difference between that study and the present study is that the XYZ data spacing in the CVM in the upper 300 m was reduced to 30 × 30 × 30 m to better match the spacing of the surface topography. Spacing transitions to 100 × ×100 × 100 m at 300 m depth, before transitioning back to 300 m spacing below 1200 m depth. After adjusting the base CVM to conform to the surface topography, the geotechnical gradient was applied.

An additional factor tested in this study was the presence of a near-fault damage zone adjacent to the Tacoma fault. Multiple studies have found that mature faults often have an associated damage zone that surrounds the fault to a depth of several kilometers and that can locally reduce seismic velocities (e.g., Li *et al.*, 2003, 2004; Cochran *et al.*, 2009; Lewis and Ben-Zion, 2010; Yang and Zhu, 2010). With respect to earthquake modeling, a low-velocity zone near the fault can produce a fault-zone waveguide that increases high-frequency shaking adjacent to the fault, while reducing high-frequency, fault-normal shaking relative to fault-parallel shaking throughout the model region (Graves and Pitarka, 2016). In addition, the damage zone may affect shallow rupture propagation by reducing

Downloaded from http://pubs.geoscienceworld.org/ssa/bssa/article-pdf/113/6/2519/6037178/bssa-2023083.1.pdf
by University of Washington user

rupture velocities, which are sensitive to the *S*-wave velocity in the fault's host rock. Because detailed, shallow velocity characterization has not been conducted across the Tacoma fault, it is unclear whether the fault hosts a distinct damage zone. However, because the fault has likely accommodated several kilometers of shortening since its creation, it is possible that a damage zone is present. To add the damage zone, we employ the method of Graves and Pitarka (2016), wherein seismic velocities are reduced by 30% within 450 m on either side of a fault, before tapering to the background velocity at 750 m from the fault. This zone extends to 4 km depth before tapering to background velocity at 6 km depth. These values represent general parameters derived from observations at a number of global crustal faults.

Though it was not explicitly considered in this study, nonlinearity would likely have a strong influence on predicted peak shaking, particularly at shorter periods of ground motion. To temper strong shaking at soft-rock sites, we imposed the minimum *S*-wave velocity of 200 m/s. This ensured that locations with initially very-low *S*-wave velocities (<200 m/s) did not produce unrealistically high shaking. All the versions of the velocity model tested were also amended in the upper kilometer such that velocity varied according to a randomized field with a standard deviation of 5% and with a characteristic wavelength of several kilometers (Frankel *et al.*, 2018). Including this variability mimics small-scale velocity variations that scatter surface waves and reduce focusing of seismic energy (Hartzell *et al.*, 2010; De Martin *et al.*, 2021; Scalise *et al.*, 2021; Lehmann *et al.*, 2022). The peak modeled frequency for the amended velocity models and mesh is estimated to be ~2.5 Hz.

RESULTS AND INTERPRETATION

To evaluate our results, we compare simulated ground motions to predictions of the 5% damped spectral acceleration (SA) values from four of the Next Generation Attenuation-West2 GMMs (Abrahamson *et al.*, 2014; Boore *et al.*, 2014; Campbell and Bozorgnia, 2014; Chiou and Youngs, 2014). These models provide an independent baseline against which we can highlight variations between different versions of the simulation, while also allowing us to compare our simulated shaking to empirically estimated shaking. In particular, we rely upon the epsilon (ε) value, defined as follows:

$$\varepsilon = \frac{\mu_{\mathrm{Sim}} - \mu_{\mathrm{GMM}}}{\sigma_{\mathrm{GMM}}}, \tag{3}$$

in which μ_{Sim} is the logarithmic mean SA for the simulated results, μ_{GMM} is the logarithmic mean of the GMM estimates, and σ_{GMM} is the logarithmic mean total standard deviation of the GMM estimates. The GMM site terms were calculated using the same V_{S30} map used for developing the geotechnical gradient, and basin terms were calculated using velocity-depth horizons derived from the unmodified CVM (e.g., Fig. 1b,c).

Unmodified CVM results

A primary goal of this work is to assess how well direct simulations perform over a wide range of frequencies, including frequencies above 1 Hz. Initial tests sought to characterize how well the unmodified CVM behaved at this frequency range. We start by looking at results from the 18 M_{w} 7.0 simulations conducted using the unmodified CVM. Figure 3a–d illustrates the average ε value with distance from the fault at 0.5, 1.0, 2.0, and 5.0 s periods (T), and Figure 3e–h also maps the average ε value within the model region. Simulated ground motions for periods greater than 1.0 s tend to be within one standard deviation of the GMM-estimated ground motions. An exception to this behavior is 5.0 s ground motion within the Tacoma basin, which is significantly amplified relative to the GMMs (strong peak starting at ~15 km). Amplification of long-period seismic waves by the Puget Sound sedimentary basins has been well documented (Rekoske *et al.*, 2021). In particular, the Seattle basin has shown a strong propensity for long-period amplification during the previous deep-focus earthquakes (Frankel *et al.*, 2002) as well as in ground-motion simulations (Frankel *et al.*, 2018; Wirth, Frankel, *et al.*, 2018; Wirth *et al.*, 2019; Thompson *et al.*, 2020; Stone *et al.*, 2022). This amplification is often greater than that predicted by GMMs. Although evidence for amplification in the Tacoma basin during the past earthquakes is sparse by comparison, it is not surprising that the simulated ground motions demonstrate amplification similar to that in the Seattle basin, considering that the basins share similar genesis, morphology, and material properties. We discuss this possible basin amplification more in the following subsection. As for ground motions at or less than 1.0 s, shaking tends to be underestimated often by more than one standard deviation; this is particularly true for 1.0 s shaking outside of the Tacoma basin and throughout the model area for 0.5 s shaking. Because these periods of shaking are sensitive to smaller scale velocity variations, they are more affected by the unnaturally high surface velocities (~500 m/s), resulting in an underestimation of shorter period shaking. This demonstrates the functional lower limit period range for performance of the unmodified CVM.

Geotechnical gradient results

Comparison with the unmodified CVM. We also evaluate ε values for the version of the velocity model with a geotechnical gradient (Fig. 4). The version of the CVM with a geotechnical gradient tends to produce peak ground motions within one standard deviation of GMM estimates at 0.5 and 1.0 s periods. The shape of the ε versus distance curves at these periods does not significantly change relative to the unmodified CVM, but the overall ground motions tend to be higher. This effect produces a slight overestimation of GMM-predicted ground

Downloaded from http://pubs.geoscienceworld.org/ssa/bssa/article-pdf/113/6/2519/6037178/bssa-2023083.1.pdf
by University of Washington user

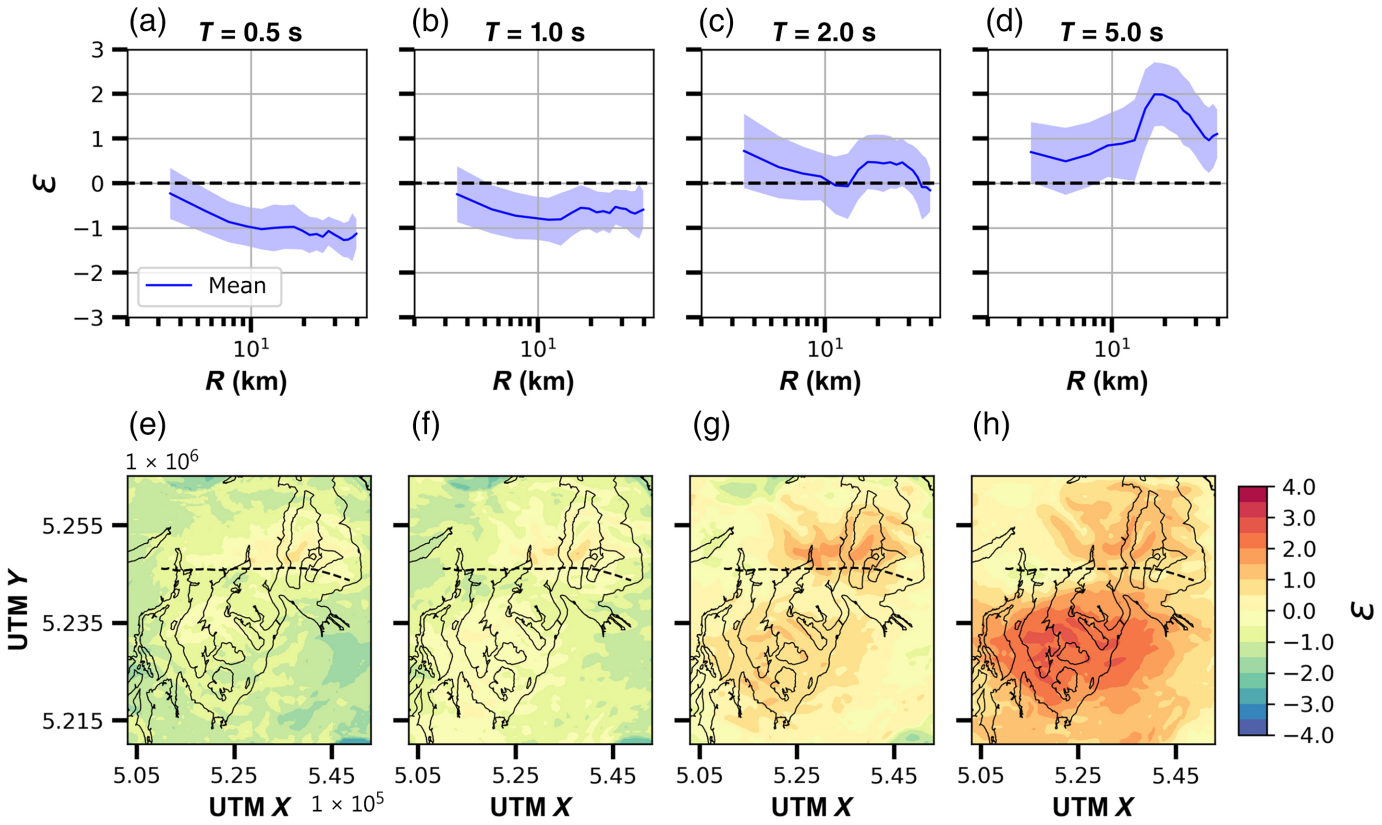

Figure 3. Epsilon (ε) comparisons for the 18 M_w 7.0 simulations conducted using the unaltered Cascadia velocity model (CVM). A value of $+1\varepsilon$ indicates ground motions one standard deviation greater than ground-motion model (GMM) estimates, and a value of -1ε indicates ground motions one standard deviation lower than GMM estimates. (a–d) ε versus closest distance to the rupture plane (R) at different periods of ground motion. (e–h) ε is mapped across the model region. The blue curve corresponds to the mean of the epsilon value in a given distance bin, and the blue shaded area represents the $\pm\sigma$ range of the epsilon values. The dashed line in the maps denotes the surface trace of the M_w 7 source. The color version of this figure is available only in the electronic edition.

motions at 1.0 and 2.0 s periods, but diminishes at 5.0 s. Precisely why ground motions are slightly overestimated at short and intermediate periods is difficult to constrain. A possible cause may be the lack of direct consideration for nonlinearity at soft-rock sites, which would primarily affect shorter period shaking (i.e., T = 0.5 and 1.0 s). However, based on the relative improvement in short-period ε values in the version of the simulations using the geotechnical gradient, we will use the geotechnical simulations as the basis for our interpretation of earthquake effects around Tacoma, as well as the base model for the other velocity model adjustments.

Distribution and variability of ground motion. Wave propagation is strongly affected by the rupture parameters in any one simulation, as well as influenced by the Tacoma basin. We plot snapshots of the vertical velocity field from an M_w 7.0 scenario with a deep, eastern hypocenter in Figure 5. Shaking initiates at the epicenter near the northeast corner of the model region and propagates outward, primarily to the southwest and toward the Tacoma basin. The strongest shaking tends to be in the forward rupture direction. High-amplitude surface waves develop on the footwall within t = 15.0 s and persist through the remainder of the simulation. These surface waves slowly propagate to the southwest, with longer wavelength components dispersing well before the shorter wavelengths. For example, at t = 45.0 s after origin time, a small packet of strong, short-wavelength surface waves can still be seen traversing the center of the basin. Moving at less than a kilometer per second, these waves are likely sampling the thick Quaternary materials layer in the basin, which has an average velocity between 600 and 700 m/s (Fig. 1b).

In Figure 6, we map the average peak ground velocity (PGV), as well as the variability in the PGV, for all 18 of the earthquake rupture scenarios. The average maximum shaking for these events is ~2.5 m/s, typically manifesting within 5 km of the fault's surface trace (Fig. 6a). PGVs remain high on the fault's hanging wall, gradually tapering to the north as the depth of the rupture plane increases. Conversely, PGVs reduce more abruptly on the footwall, dropping below 1 m/s within 5 km of the surface trace. Most areas north of Tacoma experience the maximum PGVs greater than 0.5 m/s. The interevent variability of the PGV (Fig. 6b) roughly follows the PGV

Downloaded from http://pubs.geoscienceworld.org/ssa/bssa/article-pdf/113/6/2519/6037178/bssa-2023083.1.pdf
by University of Washington user

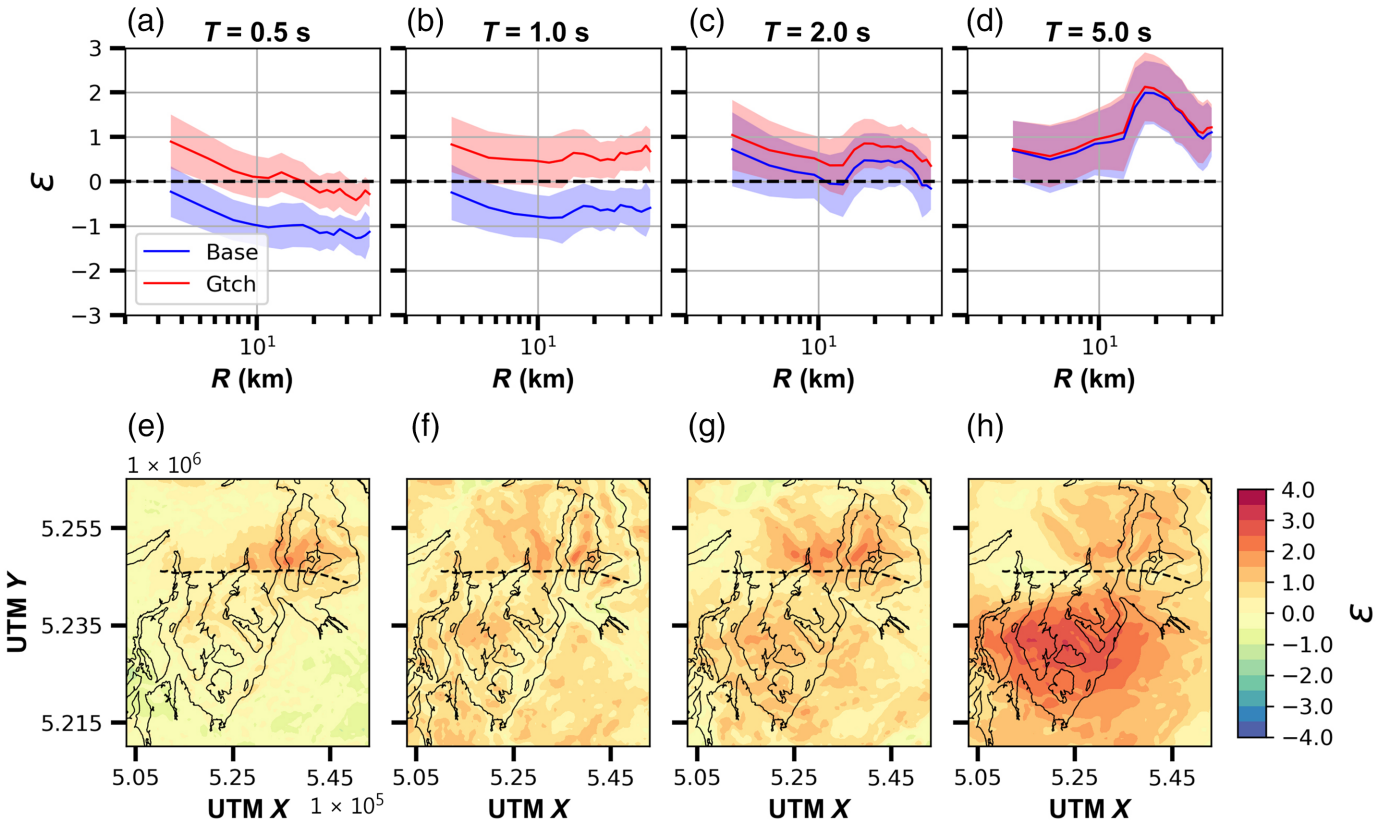

Figure 4. Epsilon (ε) comparisons for the 18 M_w 7.0 simulations conducted using the CVM amended with the geotechnical gradient. (a–d) ε versus closest distance to the rupture plane (R) at different periods of ground motion. The red curve corresponds to ε from the geotechnical simulations, and the blue curve corresponds to the standard (i.e., unaltered) CVM simulations. (e–h) ε is mapped across the model region. The color version of this figure is available only in the electronic edition.

distribution, with the greatest variability around 5 km north of the surface trace, in which it reaches the maximum of ~1 m/s.

The timing of peak shaking varies significantly at different periods of ground motion. Analysis of filtered seismograms at sites along a line extending from the fault to the south end of the model region (i.e., crossing the Tacoma basin) demonstrates that peak shaking at any one period is often associated with a coherent wavefront (Fig. 7, first row; Fig. S3 plots the north–south component of the wavefield). The PGV at a particular period is determined by band-pass filtering the seismograms in a range equivalent to $\pm 0.25 \times T^{-1}$ Hz around each period (e.g., for T = 5 s, the range is 4–6.7 s). At 0.5 and 1.0 s, these wavefronts are often composed of early arriving surface waves; though peak 1.0 s shaking often coincides with the initial *S*-wave arrival within 20 km of the fault. Shaking at 2.0 and 5.0 s is dominated by slower moving surface waves. In particular, peak 2.0 s shaking is associated with the packet of short-wavelength surface waves observed in Figure 5.

We plot the log(SA) values at periods of 0.5, 1.0, 2.0, and 5.0 s in Figure 8. Overall, shorter period ($T \leq 2.0$ s) shaking is the greatest on the hanging wall within 5 km of the surface trace (Fig. 8a–d). Longer period ($T = 5.0$ s) shaking is the greatest on the footwall within the Tacoma basin, generally reaching the maximum value 10–20 km west of Tacoma. This amplification is ostensibly related to the full thickness of sediments within the basin (as opposed to just the thickness of Quaternary sediments), because the amplification pattern mirrors the depth to the tertiary–basement interface in the basin (Fig. 1c).

The effects of forward rupture directivity become apparent when comparing the SAs between the deep (Fig. 8e–h) and middepth (Fig. 8i–l) hypocenters. At $T \geq 1.0$ s, ground shaking is typically greater in the scenarios using deep hypocenters than the middepth hypocenters. These effects are apparent on both the hanging wall and footwall. The effect largely diminishes at 0.5 s.

We explore directivity effects more in Figure 9, in which we plot the average SA values associated with the eastern, central, and western hypocenter. On the hanging wall, shaking trends higher on the side of the model corresponding to the hypocenter location for $T \leq 2.0$ s. At 5.0 s, hanging-wall shaking is higher on the side of the model opposite the hypocenter. Footwall ground motions appear more sensitive to directivity, with ground shaking at all periods remaining higher on the side of the model opposite the hypocenter.

In addition to the M_w 7.0 tests, we ran a suite of M_w 6.5 scenarios, representing a smaller earthquake on the fault. We

Downloaded from http://pubs.geoscienceworld.org/ssa/bssa/article-pdf/113/6/2519/6037178/bssa-2023083.1.pdf
by University of Washington user

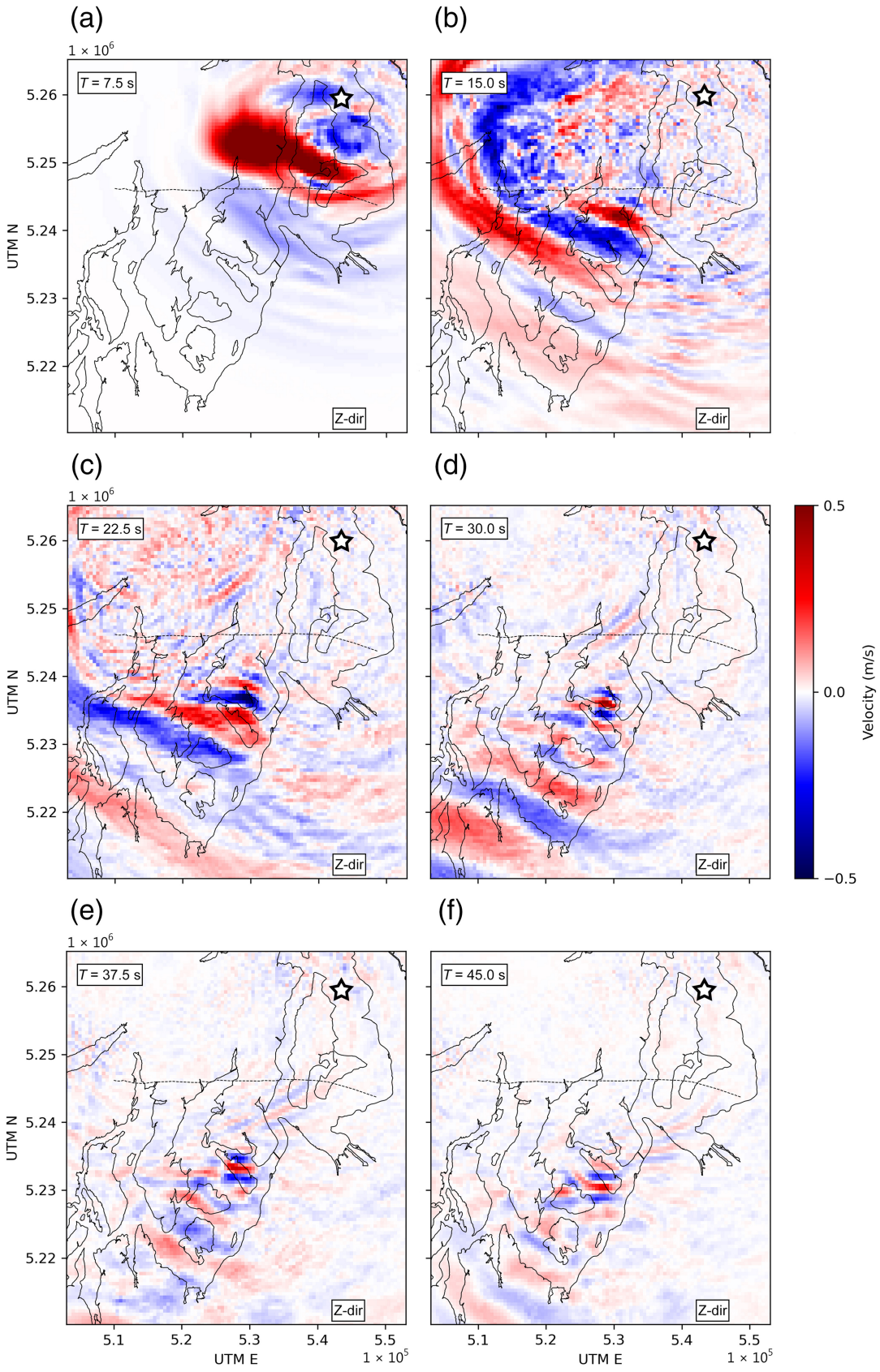

Figure 5. (a–f) Snapshots of the vertical velocity field at different times in a simulation. The simulation is for an M_w 7.0 source with an eastern, deep hypocenter (epicenter is denoted with a star). The red shading represents upward motion, and blue shading represents downward motion. The color version of this figure is available only in the electronic edition.

Downloaded from http://pubs.geoscienceworld.org/ssa/bssa/article-pdf/113/6/2519/6037178/bssa-2023083.1.pdf
by University of Washington user

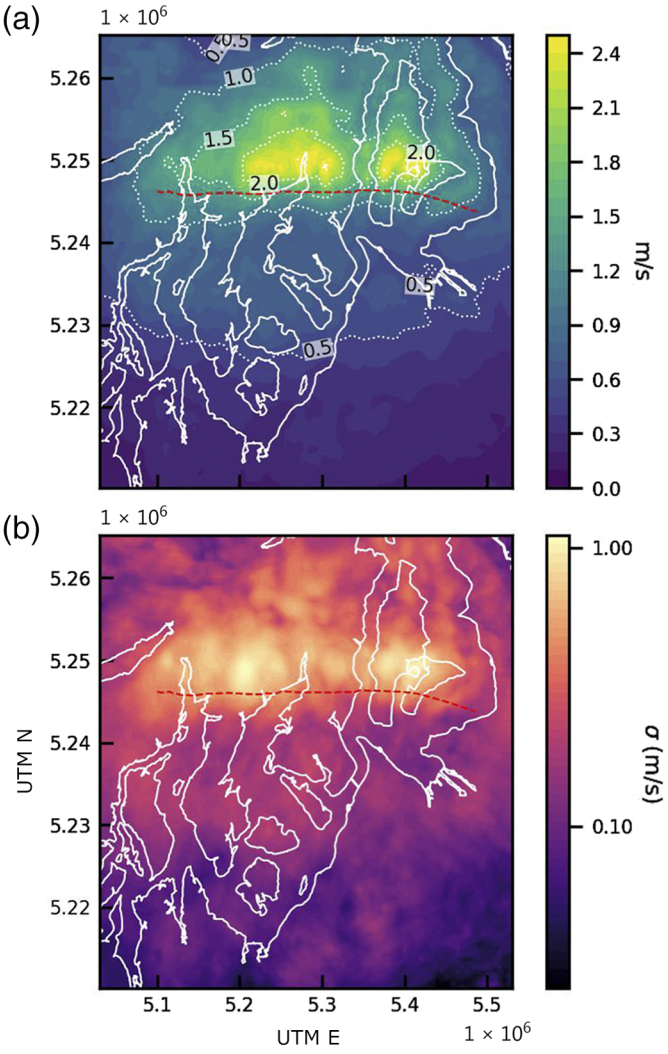

Figure 6. (a) Peak ground velocity (PGV) and (b) its standard deviation for the 18 M_w 7.0 source scenarios. The color version of this figure is available only in the electronic edition.

explore the same subset of hypocenter parameters for the M_w 6.5 tests as in the M_w 7.0 analysis in Figures S4–S8. Here, we focus on the effect of shifting the source location west and east along the fault zone. In addition to the 18 rupture scenarios run on the central M_w 6.5 source location, nine scenarios were run on source regions shifted approximately one-half source length to the west and east (Fig. 1a); this subset of scenarios only employed mid-depth hypocenters. We compare the effects of shifting the source location in Figure 10. For short-period shaking ($T \leq 2.0$ s), amplitudes are the greatest on the hanging wall within 5 km of the surface trace. For 5.0 s shaking, amplitudes tend to be the greatest in the Tacoma basin. However, the distribution of high-amplitude shaking varies significantly as the source moves along the fault zone, with the eastern source location producing the smallest region of high-amplitude shaking. In Tacoma, the strongest shaking at 0.5–1.0 s is produced by an eastern source location, and shaking is the greatest from a central source location at 2.0–5.0 s.

These results suggest the the strength of the basin response for the Tacoma basin is sensitive to the azimuth of incoming energy, reinforcing results from prior simulation-based studies (Frankel *et al.*, 2018; Wirth, Frankel, *et al.*, 2018; Wirth *et al.*, 2019). However, observational studies have noted only intermittent amplification within the Tacoma basin (if at all), with little indication that it was azimuthally dependent (Thompson *et al.*, 2020). Most observations from the Tacoma basin are from a handful of stations along its margins, at which only a small number of significant earthquakes have been recorded. The existing records do not span the full range of seismic energy that would be expected during a Tacoma fault earthquake (namely, long-period seismic waves generated by a shallow source). Furthermore, significant long-period amplification may tend to manifest above the deeper, central portions of the basin, as prior simulations have suggested (Frankel *et al.*, 2018; Wirth, Frankel, *et al.*, 2018; Wirth *et al.*, 2019). The discrepancy between observations and simulations may, therefore, be a factor of these data limitations. Another possibility is that the velocity structure of the Tacoma basin is not well represented in the CVM. Although its structure has been broadly constrained through active and passive seismic studies, finer-scale structure, like that adjacent to the Tacoma fault at the northern end of the basin, is less well resolved. More earthquake recordings and structural data from within the basin could help to address these questions.

Topographic effects

Tests with surface topography were conducted using the version of the velocity model including the geotechnical gradient. As such, the comparisons we make in this section are relative to the simulations using a flat, geotechnical velocity model.

In interacting with surface topography, seismic waves can be significantly amplified, as well as de-amplified or scattered. Conspicuous instances of topographic amplification have been observed during many earthquakes (e.g., Davis and West, 1973; Celebi, 1987; Hartzell *et al.*, 1994, 2014; Pedersen *et al.*, 1994; Spudich *et al.*, 1996; Hough *et al.*, 2010; Pischiutta *et al.*, 2010). Some case studies have found that topography can increase peak ground shaking by a factor of two or more (Geli *et al.*, 1988). However, topographic amplification is not typically considered in wave propagation modeling. This is because the effect often manifests at higher frequencies (>1 Hz), is highly variable with respect to source and topography characteristics, and is relatively difficult to parameterize in most commonly used modeling methods. With the greater availability of parallel computing resources and the advent of specialized codes like SPECFEM3D that can easily incorporate topography, it is now feasible to include surface topography in a typical waveform simulation.

The effects of topography on ground shaking during simulated finite-fault rupture were explored extensively in Stone *et al.* (2022). In that study, the authors attempted to generalize

Downloaded from http://pubs.geoscienceworld.org/ssa/bssa/article-pdf/113/6/2519/6037178/bssa-2023083.1.pdf
by University of Washington user

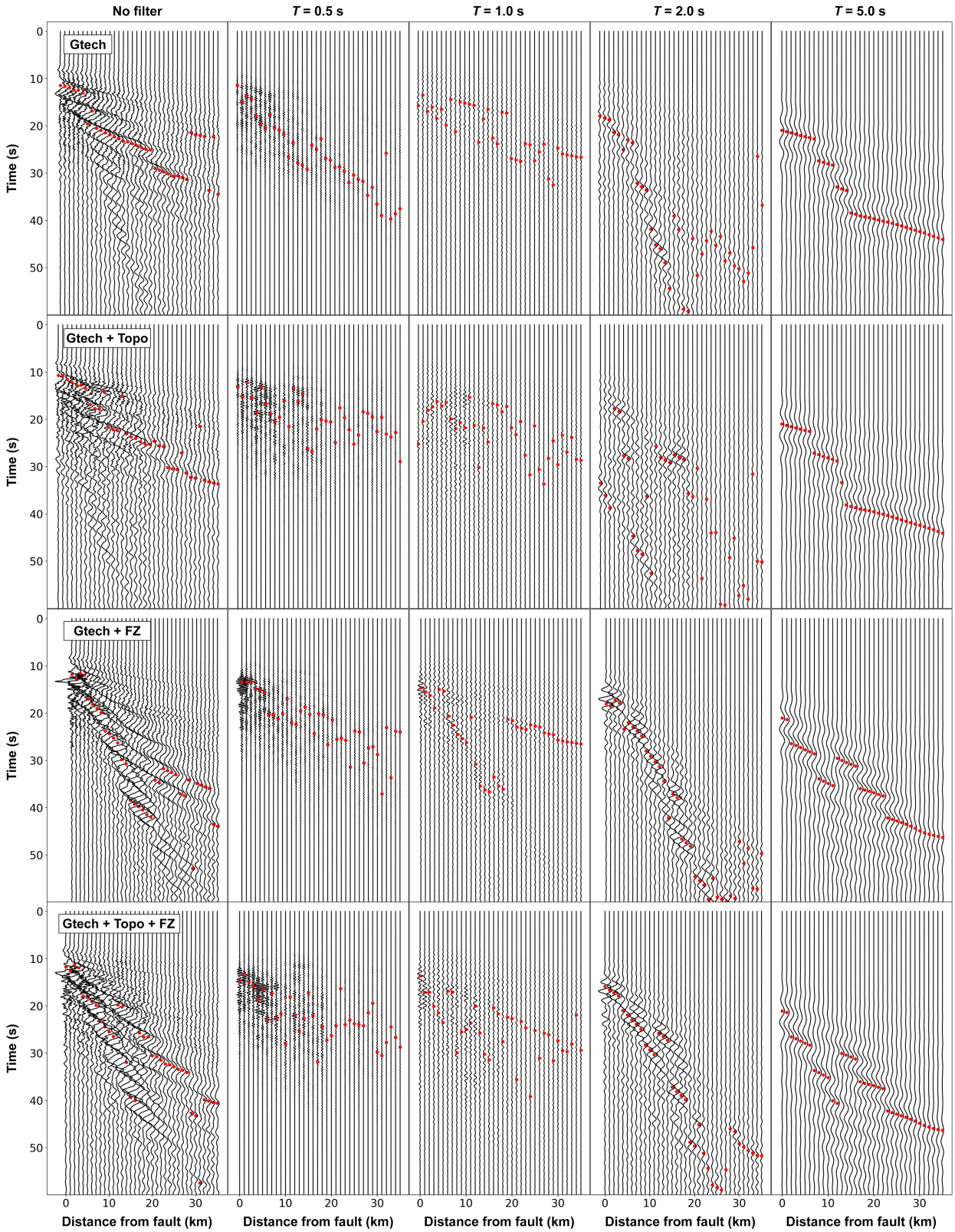

Figure 7. Vertical velocity seismograms from the source realization shown in Figure 5. Seismograms are in a north–south line extending from the fault zone to the south end of the model region, following the UTM E 525,000 value. From top to bottom, the rows correspond to the velocity model considering the geotechnical gradient, the model with the geotechnical layer and topography, the model with the geotechnical gradient and fault damage zone, and the model with all three amendments. The red dots represent the timing of the peak ground velocity for each seismometer in each period range. The color version of this figure is available only in the electronic edition.

Downloaded from http://pubs.geoscienceworld.org/ssa/bssa/article-pdf/113/6/2519/6037178/bssa-2023083.1.pdf
by University of Washington user

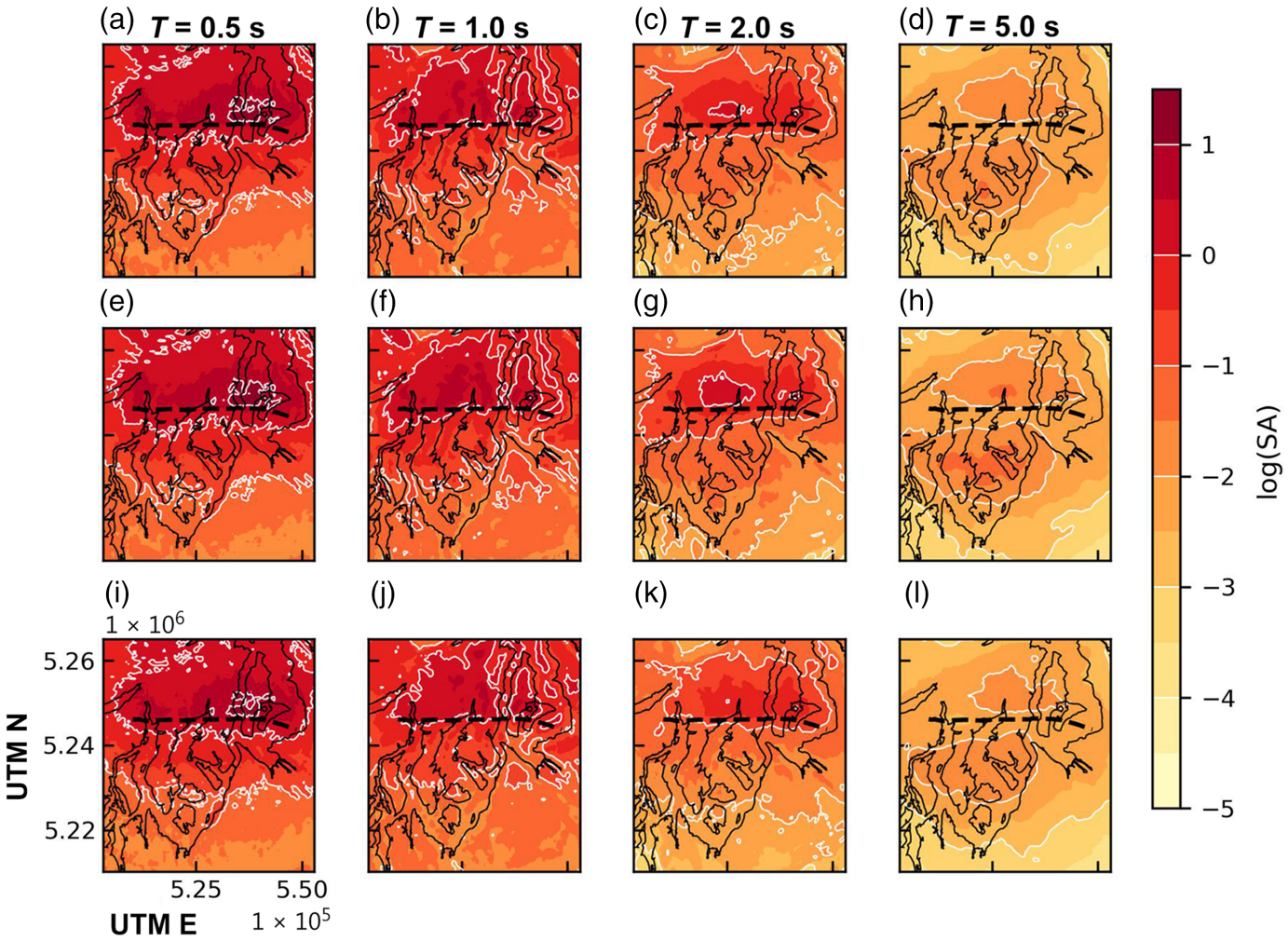

Figure 8. Logarithm of the spectral acceleration (SA) mapped for the M_w 7.0 simulations at different periods. (a–l) The rows correspond to the average of all 18 source scenarios, the average of the nine deep-depth hypocenter scenarios, and the average of the nine middepth hypocenter scenarios. The color version of this figure is available only in the electronic edition.

the effects of topography on ground shaking by simulating a suite of earthquakes on the Seattle fault, another major fault in the Puget Sound region. In the current study, we expand on those results by exploring a larger selection of rupture scenarios (18 M_w 7.0 ruptures, versus the nine used in that study). We also employ a different near-surface velocity structure in applying the geotechnical gradient. We summarize the primary observations from the current study below, but a thorough comparison to Stone *et al.* (2022) is included in the supplemental material as well.

On average, ground motions in the model with topography are similar to those in the model without topography. We plot comparisons of ε between the flat and topography model in Figure 11. The curves for ε versus distance assume similar shapes and values (Fig. 11a–d). The largest difference is associated with 2.0 s shaking, which increases at 5–25 km. Variability in the response at a given period relative to the flat model is very sensitive to the scale of topography (Fig. 11i–l). For instance, 0.5 s shaking is most sensitive to topographic features less than a kilometer in width, whereas 5.0 s shaking is predominately sensitive to features several kilometers in width. Notably, shaking amplification and de-amplification appear to strongly correlate with topographic highs and lows, respectively. The scattering effects of topography are evident in seismograms within the Tacoma basin (Fig. 7, second row). The coherent wavefronts associated with PGVs at low and intermediate periods in the flat simulations (Fig. 7, first row) are scattered in the topography simulations. In addition, shaking at any one location tends to last longer in the topography simulations, likely reflecting an abundance of backscattered energy. Comparisons of average PGV amplification in the topography simulations relative to the flat simulations (as well as the other CVM amendments) are included in Figures S9–S11.

Observed topographic amplification often manifests near a particular frequency related to the shape and average *S*-wave velocity V_S of a feature, often referred to as the topographic resonance frequency (F_r). For hills, this frequency can be generalized as $F_r = c \times V_S/L$, in which L is the basal width, and c is a constant around 0.7–1.0, depending on the height-to-width ratio

Downloaded from http://pubs.geoscienceworld.org/ssa/bssa/article-pdf/113/6/2519/6037178/bssa-2023083.1.pdf
by University of Washington user

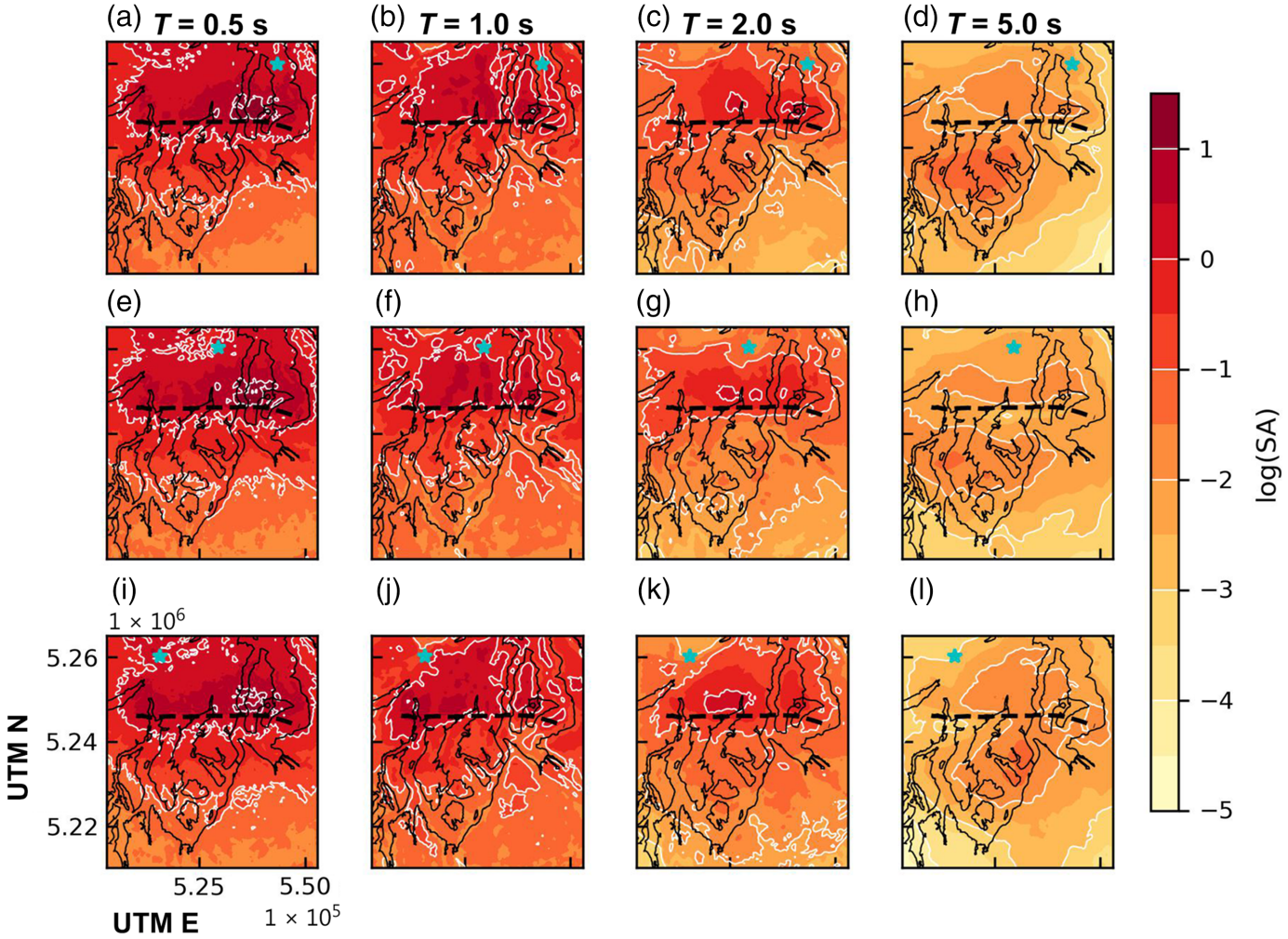

Figure 9. Logarithm of the SA mapped for the M_w 7.0 simulations, focusing on different along-strike hypocenter locations. (a–l) The rows correspond to the average of the six eastern hypocenter source scenarios, the average of the six central hypocenter scenarios, and the average of the six western hypocenter scenarios. The cyan stars represent the mapped location of each of the deep hypocenters. The color version of this figure is available only in the electronic edition.

of the hill, and whether *SV* or *SH* waves are under investigation (Paolucci, 2002). For cliffs, the equation becomes $F_r = V_S/5/h$, in which h is the height of the cliff (Ashford and Sitar, 1997). We investigate the prevalence of topographic resonance in our simulations by comparing the shaking at different periods between the top and bottom of a select set of topographic features (Fig. 12). Most of these features are coastal bluffs or cliffs, and one is a triangular ridge (Bresemann Forest). These features span a range of different heights and orientations, and so should provide a nuanced set of observations for topographic amplification. Elevation profiles across each of these features are included in Figures S12–S30.

To interrogate the presence of topographic resonance, we compare shaking between the foot, slope, and crest of each topographic feature. We show a typical topographic array (VIE2), and color stations based on the amplification of horizontal PGV at a given period relative to the station at the foot of the feature (Fig. 12c–f). Amplification values are calculated as the average percentage change in horizontal PGV between a given station and the base station in all the 18 simulations. The average V_S in this feature is 500 m/s, and the height of the feature is 152 m. Using the equation for the topographic resonance frequency of cliffs, we calculate the F_r to be 0.66 Hz (1.52 s). Topographic resonance manifests as a steady increase in amplification between the foot and crest of a feature. For VIE2, we see that this pattern manifests most strongly near 2.0 s (Fig. 12e). As such, it appears that, on average, some degree of topographic resonance is occurring in this feature. Figure 12b lists the periods at which uphill amplification is observed for each of the topographic arrays in the model region, as well as the analytically predicted resonance frequency for that feature; here, we define a positive amplification as a consistent uphill increase of at least 20%. Of the 19 observed features, 13 experience amplification in a period range consistent with their expected resonance frequencies. Conversely, there are six features that do not produce an expected amplification pattern. Some of these features are irregularly shaped or have relatively shallow slopes (e.g.,

Downloaded from http://pubs.geoscienceworld.org/ssa/bssa/article-pdf/113/6/2519/6037178/bssa-2023083.1.pdf
by University of Washington user

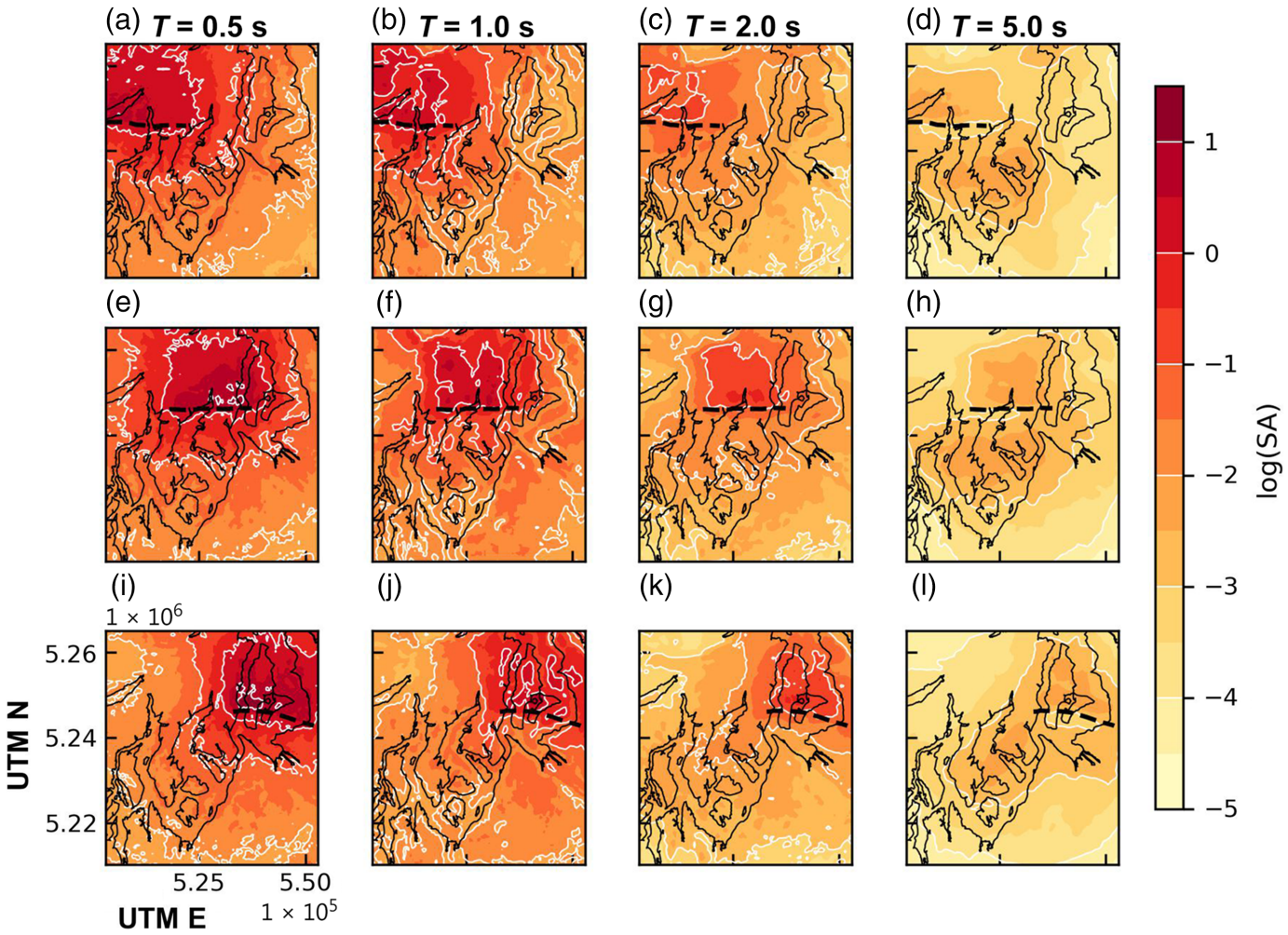

Figure 10. Logarithm of the SA mapped for the M_w 6.5 simulations, focusing on different source locations. (a–l) The rows correspond to the average of the nine western source scenarios, the average of the nine central source scenarios, and the average of the nine eastern source scenarios. The color version of this figure is available only in the electronic edition.

TAC1, TD, and TNS2), so a topographic response may be scattered or weak. For other features (e.g., HC2, HI, and TAC2), it is unclear why the observed topographic response did not match the predicted resonance frequency.

Another hallmark of topographic amplification is a tendency toward amplification in a direction perpendicular to the feature's primary axis of orientation. We examine the orientation of shaking at VIE2 using a polarization plot (Fig. 13). To develop this plot, we rotate the horizontal components of the seismogram at five-degree increments between 0° and 180°, calculating the Fourier spectra at each increment. The spectra are smoothed using a Gaussian function to reduce variability in the response. We then take the ratio of the spectra at the top of a feature over the spectra at the bottom of the feature. The resulting plots show the ratio of amplification at a range of frequencies and azimuths.

On average, the greatest shaking at the top of array VIE2 exhibits amplification of ~2.5 in the 0.6–0.7 Hz range at an orientation of ~70° east of north. This observation is consistent with the analytically predicted resonance of the feature (0.66 Hz) and occurs approximately perpendicular to the feature's primary axis of orientation (~325°). However, variability in the response is high. For example, at VIE2, it is rare that the peak observed amplification for any one given source is at the analytically predicted frequency and orientation (polarization plots for all 18 M_w 7.0 earthquake scenarios at VIE2 are included in Figs. S31 and S32). Ground motion is often greater at higher frequencies and other orientations. However, these anomalies are specific to particular hypocenters and slip distributions, and rarely manifest across multiple simulations. In other words, the topographic response at 0.66 Hz and 70° is reliably elevated, but that does not preclude more intense amplification at different frequencies and orientations during any one scenario.

Fault damage zone effects

Previous studies have shown that a fault damage zone can reduce the amplitude of high-frequency, fault-normal shaking relative to fault-parallel shaking throughout the model region

Downloaded from http://pubs.geoscienceworld.org/ssa/bssa/article-pdf/113/6/2519/6037178/bssa-2023083.1.pdf
by University of Washington user

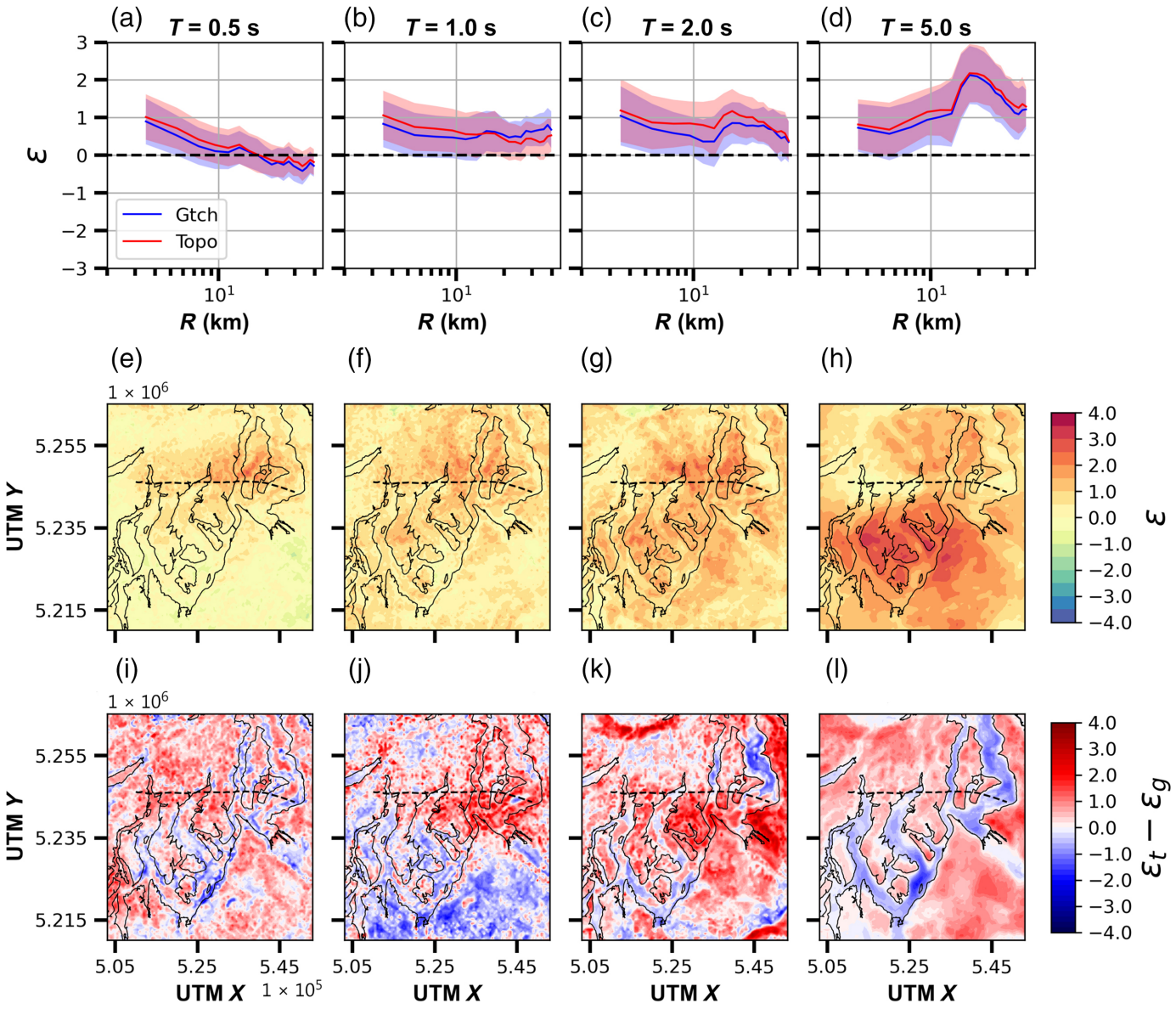

Figure 11. Epsilon (ε) comparisons for the 18 M_w 7.0 simulations conducted using the geotechnical CVM amended with topography. (a–d) ε versus closest distance to the rupture plane (R) at different periods of ground motion. The red curve corresponds to ε from the simulations using topography, and the blue curve corresponds to the flat geotechnical simulations. (e–h) ε is mapped across the model region. (i–l) The difference in ε between the topography simulations and flat simulations. The color version of this figure is available only in the electronic edition.

(Graves and Pitarka, 2016). It was hypothesized that this effect resulted from multipathing and scattering of seismic waves within the fault zone, which interrupted the coherency of high-frequency radiation patterns. Ground shaking within the fault zone was higher than outside the fault zone, particularly at higher frequencies. These findings mirror observations of wave behavior in real-world fault zones, in which seismic waves may be trapped and amplified in low-velocity waveguides (e.g., Li *et al.*, 2003, 2004; Cochran *et al.*, 2009; Lewis and Ben-Zion, 2010; Yang and Zhu, 2010).

The effects of a fault damage zone in our simulations are presented in Figure 14. Relative to the standard geotechnical model, shaking at 0.5 s is higher within the damage zone (Fig. 14e–h). Away from the damage zone, the changes in short-period shaking vary depending on whether a site is on the hanging wall or footwall. Hanging-wall sites see a distinct reduction in shaking, with the greatest reduction occurring in the region directly north of the damage zone. This causes the average 0.5 s shaking within 10 km of the damage zone to reduce toward GMM estimates relative to the nondamage zone results. On the footwall, shaking is either unchanged or slightly enhanced within 20 km of the surface trace, before reducing relative to the nondamage zone results at larger distances. At more intermediate periods (1.0–2.0 s), shaking behavior on the hanging wall is like that observed at 0.5 s, with enhanced shaking within the damage zone, and reduced shaking directly north of the damage zone. However, on the footwall shaking is

Downloaded from http://pubs.geoscienceworld.org/ssa/bssa/article-pdf/113/6/2519/6037178/bssa-2023083.1.pdf
by University of Washington user

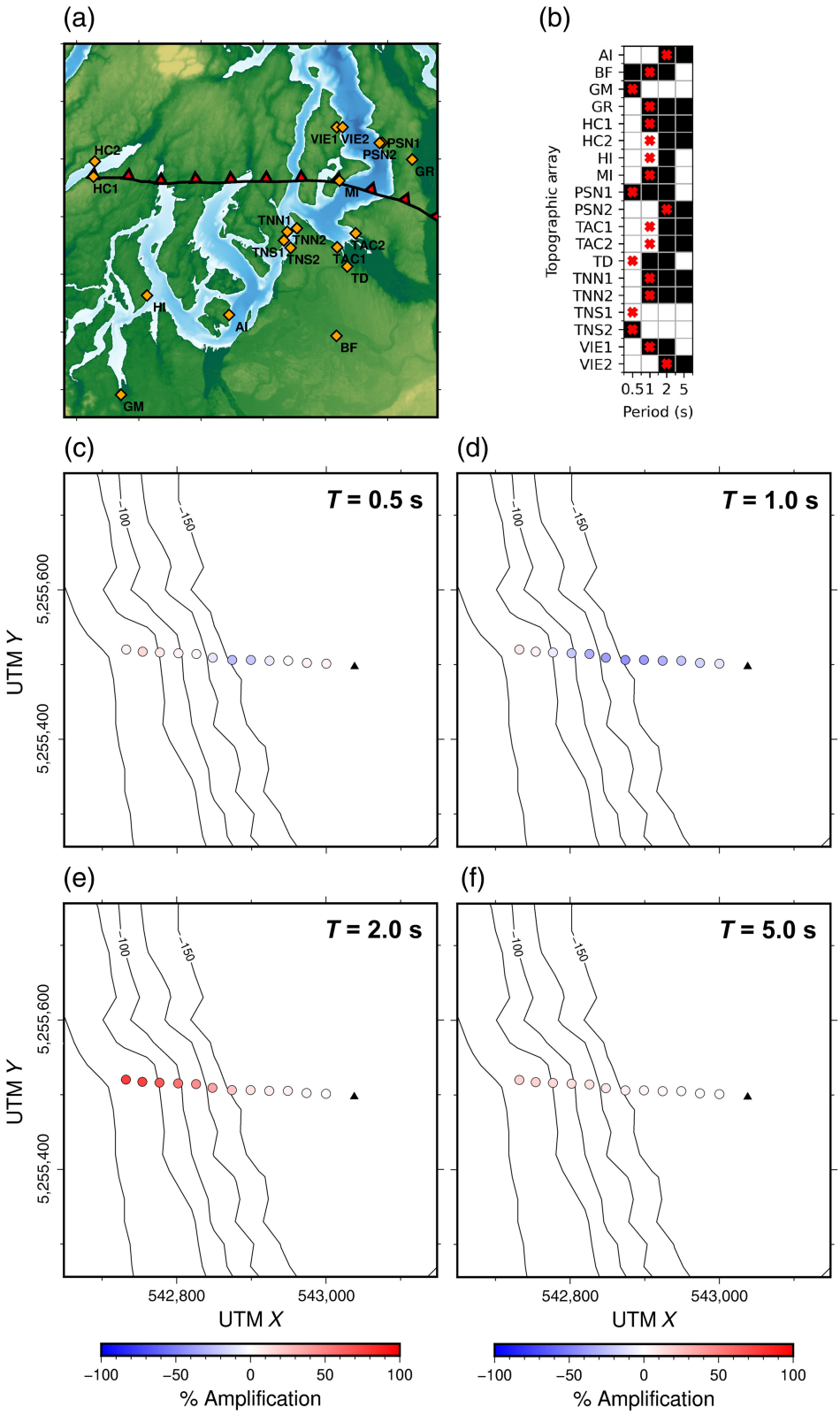

Figure 12. Average peak ground velocity comparisons at targeted topographic arrays. (a) Location of virtual topographic arrays within the model region. (b) Chart describing the periods at which sustained uphill amplification is observed. The squares filled in with black indicate observed uphill amplification at that particular array and period combination. The red crosses correspond to the analytically predicted resonance period range for that array. Amplification is determined by calculating the horizontal PGV at each slope and peak station in the array, and dividing by the PGV at a reference station in the array. Uphill amplification of at least 20% is necessary for a positive identification. (c–f) Average horizontal PGV amplification at various periods for each station in the VIE2 array. The black triangle represents the reference station. Contours denote elevation, with negative values corresponding to elevation below the sea level. The color version of this figure is available only in the electronic edition.

Downloaded from http://pubs.geoscienceworld.org/ssa/bssa/article-pdf/113/6/2519/6037178/bssa-2023083.1.pdf
by University of Washington user

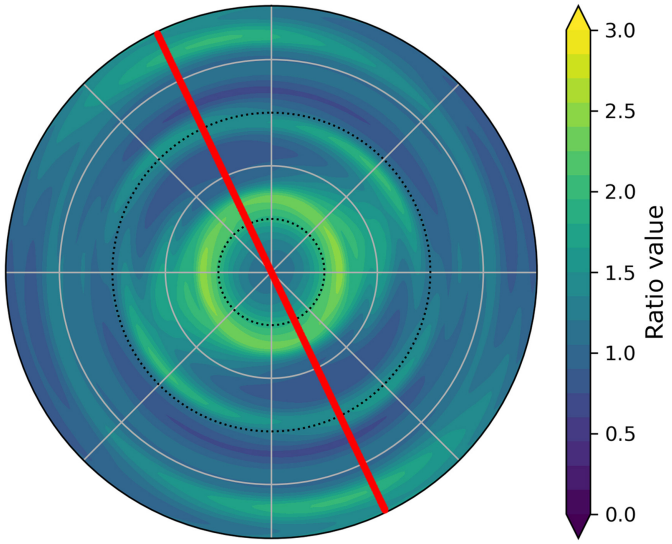

Figure 13. Average polarization of horizontal spectral ratios on the cliff near Vashon Island (array VIE2). Ratios are calculated by dividing the rotated spectral response from the station at the top of the cliff by the spectral response at the bottom of the cliff. Frequency increases outward from the center of the plot, whereas azimuths correspond to compass directions. Concentric rings mark 0.5 Hz intervals, with the innermost dotted ring representing 0.5 Hz and the outer edge of the plot representing 2.5 Hz. The colors correspond to the value of the spectral ratio at a particular frequency and azimuth. Ratio values greater than one represent amplification relative to the bottom station, whereas values less than one represent de-amplification. The red line corresponds to the primary axis of orientation of the cliff (~325°). The color version of this figure is available only in the electronic edition.

significantly enhanced relative to that observed in the nondamage zone results, particularly in the Tacoma basin. At 5.0 s, the average shaking appears to be close in amplitude to that in the nondamage zone model, except at the southern end of the Tacoma basin where shaking is amplified.

We examine the propagation of energy across the basin in Figure 7 (third row). As expected, short-period shaking is amplified within the damage zone, but is generally less organized as it propagates across the basin, as supported by the loss of coherence in the 0.5 s PGV. In the nondamage zone model, 0.5 s PGV is associated with one or two dominant wavefronts; in contrast, 0.5 s PGV in the damage zone model is not associated with any one component of the wavefield, particularly at sites >20 km from the fault. For 1.0 s shaking in the damage zone model, PGVs within 20 km of the fault are associated with a much slower moving package of surface waves than in the nondamage zone model. This same package of waves is associated with the 2.0 s shaking PGVs in both the models, though the amplitude of shaking is much greater in the damage zone model. About 5.0 s shaking is less coherent but has a slightly larger amplitude.

We suggest that the increase in shaking in the Tacoma basin at intermediate and long periods is a result of the damage zone waveguide. Because of the Tacoma fault's reverse-faulting mechanism, energy is already preferentially projected up the fault plane toward the ground surface. In adding the damage zone, this energy pulse is more efficiently directed along the fault plane and toward the surface and the footwall, enhancing surface-wave amplification in the basin. This assertion is supported by the shift of 1.0 s PGVs to a much slower wavefront; these slower propagating surface waves have shorter wavelengths and thus sample shallower materials. This suggests more coherent 1.0–2.0 s energy is making it into the basin's shallow Quaternary sediment layer, which is ~200 m thick at the fault zone and is <600 m thick in most of the basin.

To judge the sensitivity of the amplification effect to fault zone parameters, we compare shaking from simulations using three variations of the fault damage zone velocity model (Fig. 15): the original damage zone with a 1.5 km width; a version with a half-width damage zone (0.75 km); and a version without a damage zone in the velocity model, but using the same finite-fault source as the other two fault zone tests. In halving the fault zone width, the response is only marginally reduced, suggesting that the effect of the fault zone is somewhat insensitive to its width for the observed periods. The amplification patterns present in the simulations using the fault zone largely dissipate once the zone is removed, suggesting that the amplification within the basin is intrinsically tied to the presence of the damage zone.

It is also worth noting that the reduction in short-period shaking on the hanging wall appears to result primarily from the reduction in rise times within the shallow portion of the fault damage zone, as evidenced in Figure 15i,j.

Fault damage zone and topography effects

In combining all the adjustments to the velocity model, we can investigate how and to what extent each component affects response, as well as how they influence one another. Figure 16 illustrates the ε values associated with simulations run with both the topography and damage zone adjustments. From looking at the ε and ε difference maps (Fig 16e–l), the effects of both topography and the damage zone are apparent. Ground motion in the damage zone is elevated at low and intermediate periods, whereas topography amplifies and de-amplifies shaking at topographic highs and lows. However, the degree to which each of the adjustments affects shaking depends both on period and location within the model region. We plot the curves for the topography and damage zone simulations individually along with the curves for the damage zone and topography (FZtopo), and plain geotechnical simulations in the ε versus distance plots (Fig. 16a–d). At 0.5 s, the FZtopo curve trends closer to the average damage zone curve than to the topography curve, suggesting that the scattering behavior associated with the damage zone has greater influence on the average amplitude of short-period shaking than that associated with topography, though it is evident from the ε difference map that topography still influences response on cliffs and in

Downloaded from http://pubs.geoscienceworld.org/ssa/bssa/article-pdf/113/6/2519/6037178/bssa-2023083.1.pdf
by University of Washington user

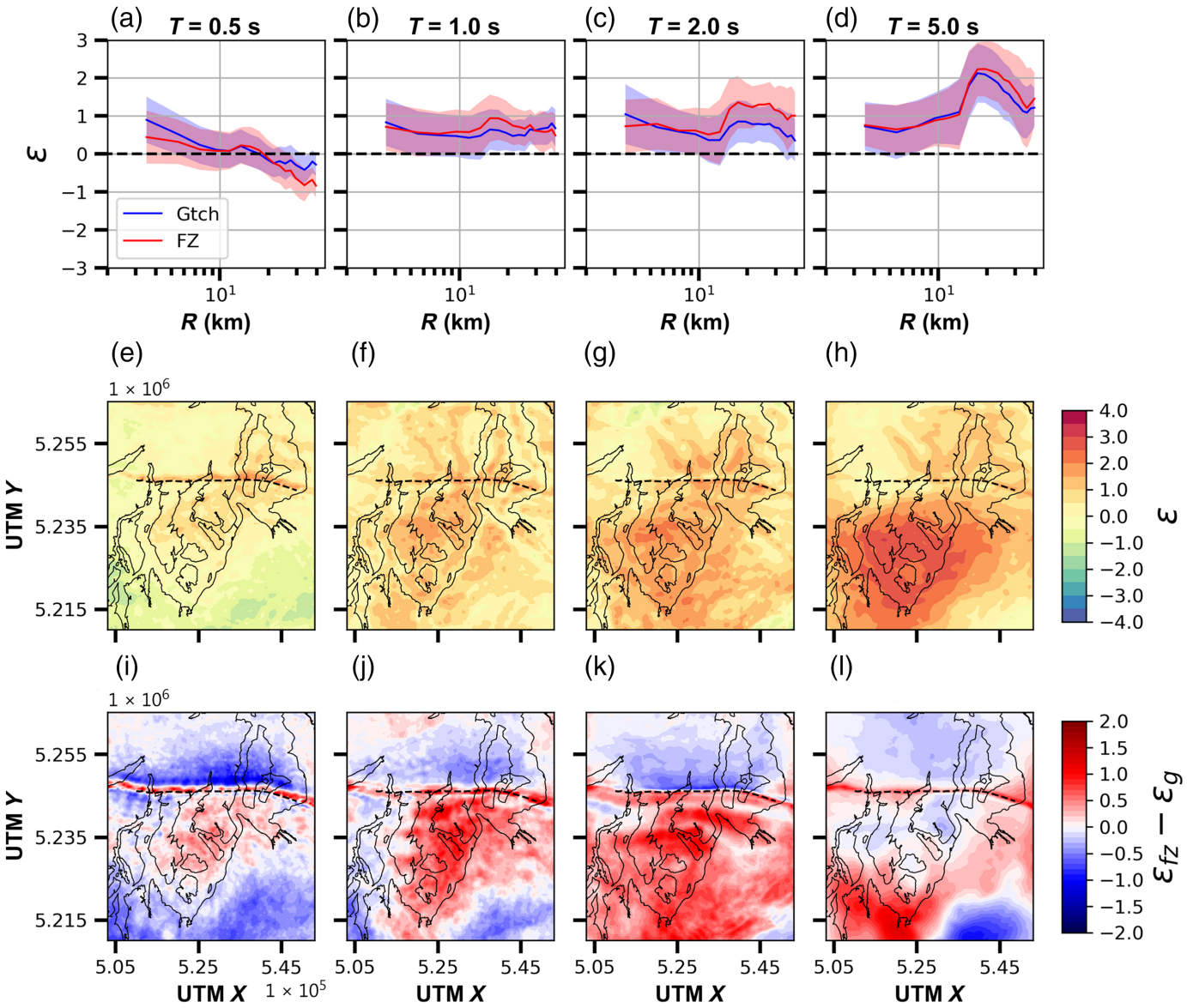

Figure 14. Epsilon (ε) comparisons for the 18 M_w 7.0 simulations conducted using the geotechnical CVM amended with a fault damage zone. (a–d) ε versus closest distance to the rupture plane (R) at different periods of ground motion. The red curve corresponds to ε from the simulations using the damage zone, and the blue curve corresponds to the nondamage zone simulations. (i–l) The difference in ε between the damage zone simulations and nondamage zone simulations. The color version of this figure is available only in the electronic edition.

valleys. At 1.0 s, the FZtopo curve assumes values much closer to the topography simulation between 5 and 20 km from the fault. Interestingly, the average value for the FZtopo curve beyond 20 km is notably lower than either the topography or damage zone curve alone. This suggests there is a factor influenced by each adjustment that results in a significant reduction in shaking. Referring back to Figure 7 (third row), 1.0 s PGVs in the damage zone simulation are primarily split between two coherent surface wavefronts. Shaking within 20 km of the damage zone is dominated by a slower moving (and thus shorter wavelength) surface wavefront, whereas shaking beyond 20 km is dominated by a faster moving (longer wavelength) surface wavefront. We suggested that the coherency of these surface waves was a result of the damage zone waveguide channeling energy more efficiently to the surface. If it is true that more 1.0 s energy is traveling close to the surface, then it may be more sensitive to scattering by surface topography. Relative to the damage zone simulation, both 0.5 and 1.0 s shaking appear to be more scattered (Fig. 7, fourth row). Both of the wavefronts associated with PGV at 1.0 s in the damage zone simulation are scattered, resulting in a loss of coherency.

At 2.0 s, average shaking closely follows the topography curve out to 15 km. Beyond 15 km, response is more similar to the damage zone curve. This corresponds to the region in which basin response was amplified in the damage zone simulations. Finally, at 5.0 s, the average shaking favors both the

Downloaded from http://pubs.geoscienceworld.org/ssa/bssa/article-pdf/113/6/2519/6037178/bssa-2023083.1.pdf
by University of Washington user

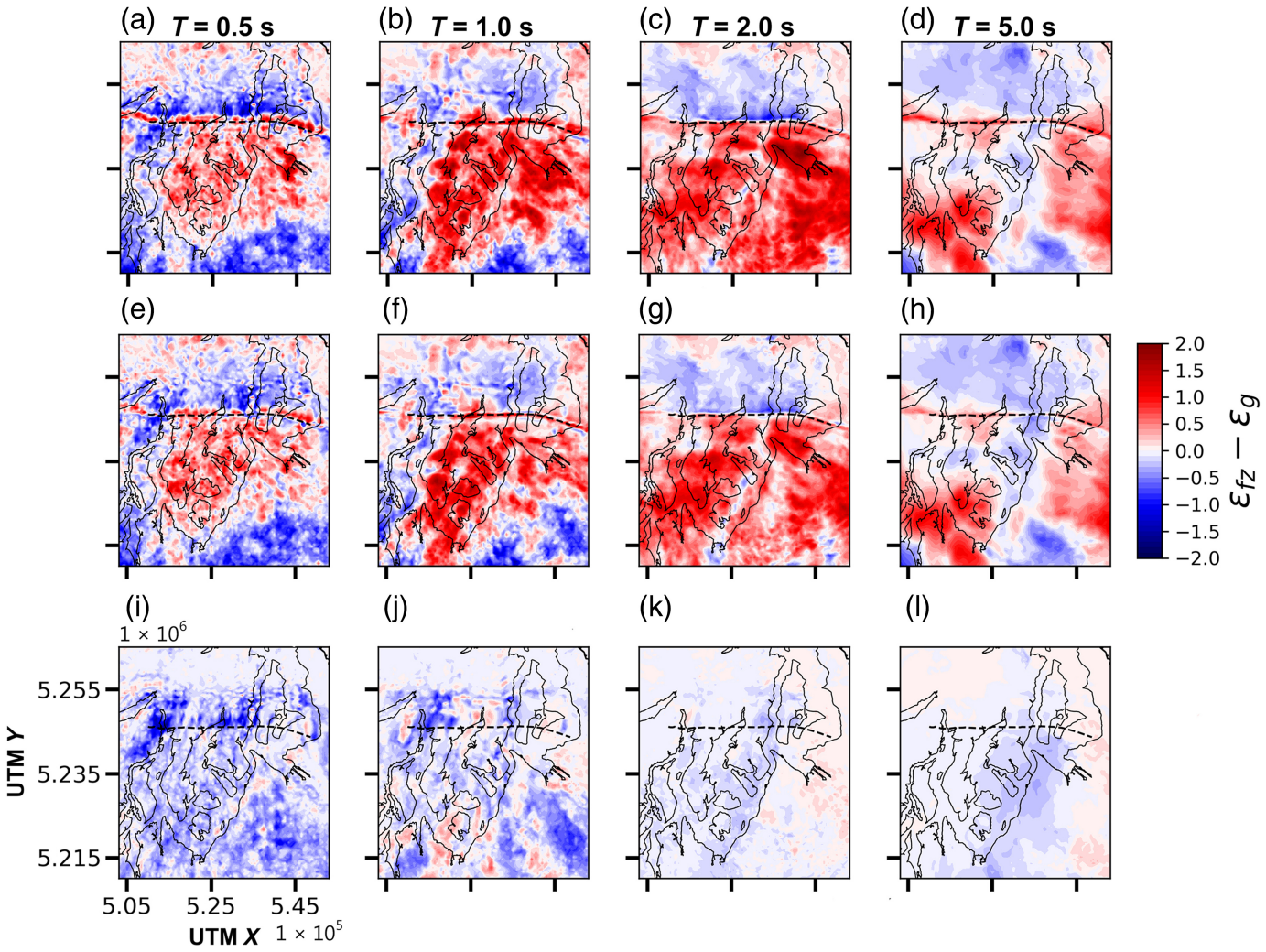

Figure 15. Epsilon (ε) difference maps considering different configurations of a fault damage zone. (a–d) Considers the original width damage zone of 1.5 km. (e–h) Considers a half-width damage zone of 0.75 km. (i–l) Considers a model that does not have a damage zone, but employs the damage zone source model (i.e., with reduced shallow rise times and moments). The color version of this figure is available only in the electronic edition.

topography and damage zone curves, even slightly surpassing both at distances greater than 20 km.

To examine the dependency of the topographic and fault zone effects at a finer scale, we plot uphill amplifications for two topographic features in Figure 17. The Governor's Mansion (GM) array spans a 40 m tall cliff near the south end of the model region, and its estimated resonance frequency is 1.75 Hz (0.57 s). The Anderson Island (AI) array spans a 200 m tall cliff in the south-central portion of the Tacoma basin, and its estimated resonance frequency is 0.45 Hz (2.2 s). Both the features typically experienced uphill amplification near these frequencies in the topographic simulations (Fig. 17a,b). The addition of the fault zone affects the strength of the topographic response on both the features. At GM, the uphill shaking at 0.5 s reduces by 37%, likely a reflection of the scattering and attenuation effects the fault zone has on short-period energy. In contrast, uphill shaking at 2.0 s increases by 89% at AI, likely because the fault zone seems to enhance the generation of midperiod surface waves in the Tacoma basin. These results reinforce the notion that modeled topographic effects are extremely sensitive to source variations and even far-field velocity model variation.

CONCLUSIONS

In this study we estimated shaking from a range of scenario M_w 6.5–7.0 earthquakes on the Tacoma fault. This included 18 different M_w 7.0 source configurations spanning three hypocenter locations, two hypocenter depths, and three slip distributions, as well as a variety of M_w 6.5 source realizations. Results from the simulations suggest that shaking from a Tacoma fault earthquake would tend to be the greatest in a region extending from the southern suburbs of Seattle to Tacoma. Ground motions demonstrate a strong dependence on response period; notably, we observe a strong, long-period (5.0 s) amplification within the Tacoma basin, 10–20 km west of Tacoma. High-amplitude, slow-moving surface waves are generated at the

Downloaded from http://pubs.geoscienceworld.org/ssa/bssa/article-pdf/113/6/2519/6037178/bssa-2023083.1.pdf
by University of Washington user

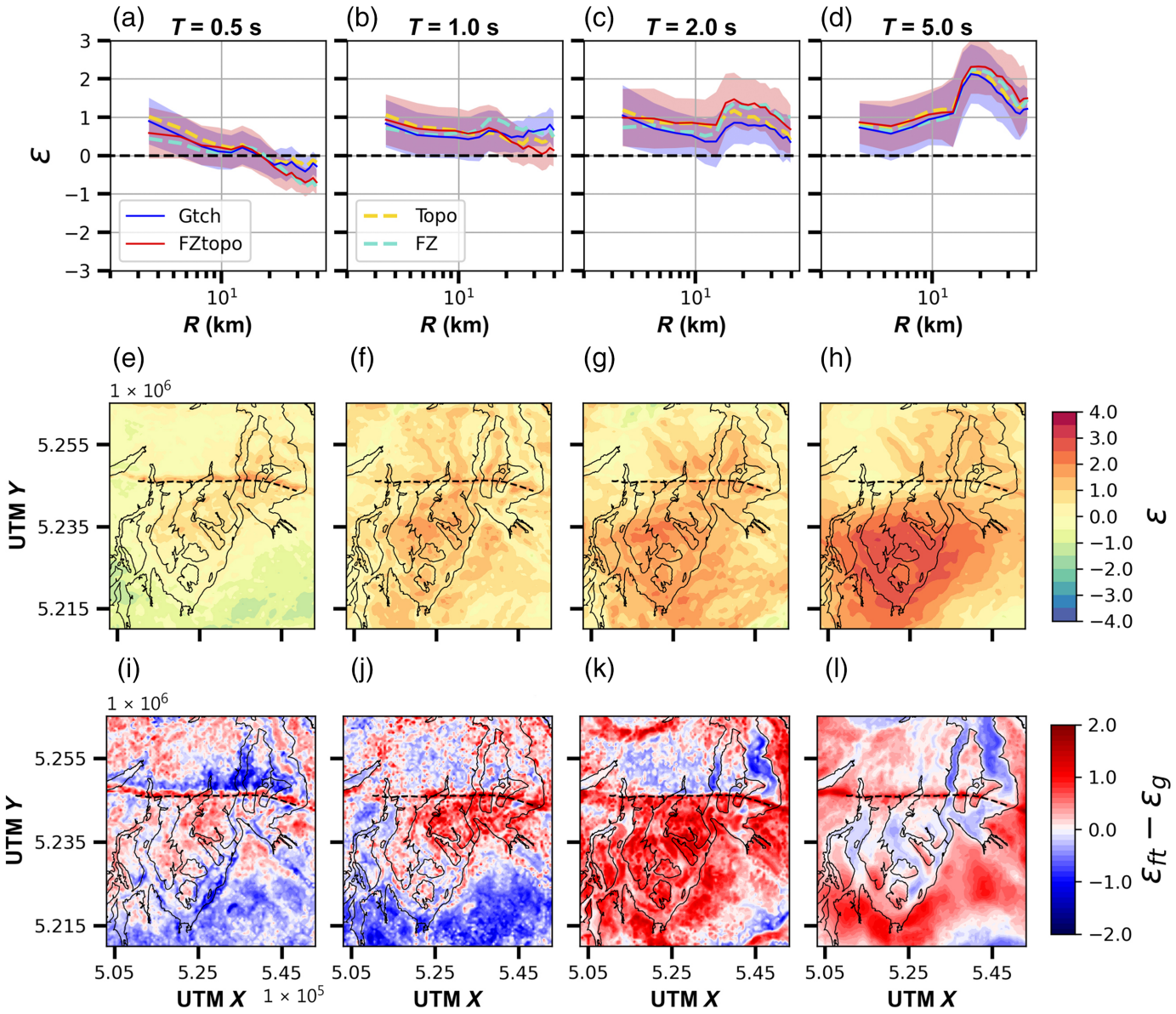

Figure 16. Epsilon (ε) comparisons for the 18 M_w 7.0 simulations conducted using the geotechnical CVM amended with both topography and a fault damage zone. (a–d) ε versus closest distance to the rupture plane (R) at different periods of ground motion. The red curve corresponds to ε from the simulations using all the three amendments, and the blue curve corresponds to the plain geotechnical simulations. We additionally plot the ε versus distance curves for the topography simulations (purple dotted line) and the fault damage zone simulations (cyan dotted line). (i–l) The difference in ε between the damage zone + topography simulations and plain geotechnical simulations. The color version of this figure is available only in the electronic edition.

north end of the basin that propagate south through the central portion of the basin. The highest amplitude waves tend to have a dominant energy around 1.0–2.0 s. The location and strength of peak ground motions in any one scenario are very dependent on source parameters, including hypocenter location, hypocenter depth, and slip distribution. A large component of this variability results from directivity effects. Changing the source location appears to influence the strength of the amplification effect within the Tacoma basin.

In addition to running a baseline set of scenarios to characterize the variability of response from large earthquakes on the Tacoma fault, we tested updates to the CVM for use in high-frequency simulations. The addition of a region-specific geotechnical gradient significantly reduced the misfit between simulated 0.5 s ground motions and empirical GMM estimates. The addition of surface topography resulted in period-dependent amplification and de-amplification at the top and bottom of cliffs and valleys, respectively. The majority of monitored topographic features typically experience amplification at or near analytically predicted topographic resonance frequencies. However, variability in this response is high and does not preclude amplification at different frequencies from one scenario to another. These results broadly agree with those of Stone

Downloaded from http://pubs.geoscienceworld.org/ssa/bssa/article-pdf/113/6/2519/6037178/bssa-2023083.1.pdf
by University of Washington user

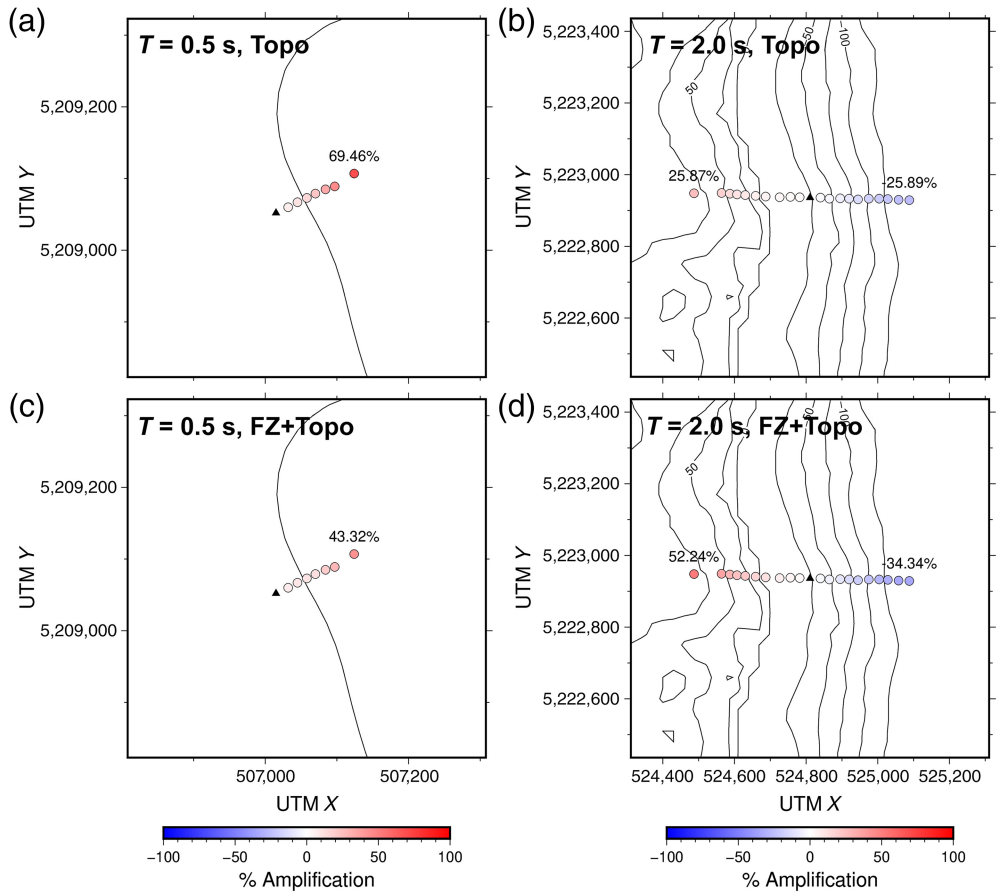

Figure 17. Average topographic amplification at the (a,c) Governor's Mansion (GM) array at 0.5 s and the (b,d) Anderson Island (AI) array at 2.0 s. (a,b) The simulations using only topography. (c,d) The simulations using a fault zone and topography. GM is a cliff that is 40 m tall, and AI is a cliff that is 200 m tall. The black triangles represent the reference stations. Contours denote elevation, with negative values corresponding to elevation below sea level. Plotted percentage values describe amplification relative to the reference stations. The color version of this figure is available only in the electronic edition.

et al. (2022)—another study focusing on the effects of topography in finite-fault simulations in the same region. Adding a near-fault damage zone resulted in amplification of short-period shaking adjacent to the fault but rapid attenuation away from the fault. The damage zone appears to improve the generation of intermediate-period (1.0–2.0 s) surface waves, likely through the effect of a low-velocity waveguide. This results in increased shaking at these periods within the Tacoma basin. When both the topography and fault zone amendments are applied in the same model, shaking behavior tends to favor one amendment or the other, depending on period and location within the model region. However, there are instances when the effects of both the amendments either combine constructively or destructively to enhance or reduce shaking. For instance, 0.5 s energy that is attenuated on account of the fault zone results in a reduction in average topographic amplification on features with predicted resonances near that period.

The results of these tests emphasize the importance of adjusting velocity models to consider high-frequency shaking. As access to high-performance computing becomes more ubiquitous and simulations are pushed to higher resolutions, these changes may prove to be critical for producing accurate ground motion predictions. As was demonstrated in this study, changes that are expected to primarily affect high-frequency shaking can have notable effects on long-period shaking as well.

DATA AND RESOURCES

The supplemental material accompanying this article contains an example profile comparing the original Cascadia velocity model (CVM) and the CVM amended with the geotechnical gradient; a full description of the results for the simulations run using an M_w 6.5 source; seismograms profiles across the Tacoma basin (north–south component); peak ground velocity (PGV) amplification distributions for each of the CVM amendments; additional comparison of the topographic simulation results with Stone *et al.* (2022); elevation profiles across the topographic seismogram arrays; and polarization plots for each of the 18 M_w 7.0 earthquake scenarios at VIE2. Simulations in this article were run using Computational Infrastructure for Geodynamics code SPECFEM3D Cartesian (Komatitsch *et al.*, 2004) available at https://geodynamics.org/resources/specfem3dcartesian/about (last accessed April 2023). All the simulations were run on the U.S. Geological Survey (USGS') Denali supercomputer (Falgout *et al.*, 2019). All the data used in this article came from published sources listed in the references.

DECLARATION OF COMPETING INTERESTS

The authors acknowledge that there are no conflicts of interest recorded.

ACKNOWLEDGMENTS

The authors would like to thank Sean Ahdi, Filippo Gatti, and an anonymous reviewer for reviewing the article and providing helpful suggestions. Any use of trade, firm, or product names is for descriptive purposes only and does not imply endorsement by the U. S. Government.

REFERENCES

Abrahamson, N. A., W. J. Silva, and R. Kamai (2014). Summary of the ASK14 ground motion relation for active crustal regions, *Earthq. Spectra* **30,** no. 3, 1025–1055, doi: 10.1193/070913EQS198M.

Downloaded from http://pubs.geoscienceworld.org/ssa/bssa/article-pdf/113/6/2519/6037178/bssa-2023083.1.pdf
by University of Washington user

Ahdi, S. K., J. P. Stewart, T. D. Ancheta, D. Y. Kwak, and D. Mitra (2017). Development of Vs profile database and proxy-based models for Vs30 prediction in the Pacific northwest region of North America, *Bull. Seismol. Soc. Am.* **107,** no. 4, 1781–1801, doi: 10.1785/0120160335.

Allstadt, K., J. E. Vidale, and A. D. Frankel (2013). A scenario study of seismically induced landsliding in Seattle using broadband synthetic seismograms, *Bull. Seismol. Soc. Am.* **103,** no. 6, 2971–2992, doi: 10.1785/0120130051.

Ashford, S. A., and N. Sitar (1997). Analysis of topographic amplification of inclined shear waves in a steep coastal bluff, *Bull. Seismol. Soc. Am.* **87,** no. 3, 692–700.

Boore, D. M., J. P. Stewart, E. Seyhan, and G. M. Atkinson (2014). NGA-West2 equations for predicting PGA, PGV, and 5% damped PSA for shallow crustal earthquakes, *Earthq. Spectra* **30,** no. 3, 1057–1085, doi: 10.1193/070113EQS184M.

Brocher, T. M., R. J. Blakely, and R. E. Wells (2004). Interpretation of the Seattle Uplift, Washington, as a passive-roof duplex, *Bull. Seismol. Soc. Am.* **94,** no. 4, 1379–1401, doi: 10.1785/012003190.

Brocher, T. M., T. Parsons, R. J. Blakely, N. I. Christensen, M. A. Fisher, and R. E. Wells (2001). Upper crustal structure in Puget Lowland, Washington: Results from the 1998 seismic hazards investigation in Puget Sound, *J. Geophys. Res.* **106,** no. B7, 13,541–13,564, doi: 10.1029/2001jb000154.

Brocher, T. M., B. L. Sherrod, E. A. Barnett, K. M. Haller, S. Y. Johnson, R. J. Blakely, D. J. Lidke, and Compilers (2016). Fault number 581, Tacoma fault, in Quaternary fault and fold database of the United States, U. S. Geological Survey, available at https://earthquake.usgs.gov/cfusion/qfault/show_report_AB_archive.cfm?fault_id=581&section_id= (last accessed October 2022).

Brune, J. N. (1970). Tectonic stress and the spectra of seismic shear waves from earthquakes, *J. Geophys. Res.* **75,** no. 26, 4997–5009, doi: 10.1029/JB075i026p04997.

Bucknam, R. C., E. Hemphill-Haley, and E. B. Leopold (1992). Abrupt uplift within the past 1700 years at southern Puget Sound, Washington, *Science* **258,** no 5088, 1611–1614.

Campbell, K. W., and Y. Bozorgnia (2014). NGA-West2 ground motion model for the average horizontal components of PGA, PGV, and 5% damped linear acceleration response spectra, *Earthq. Spectra* **30,** no. 3, 1087–1114, doi: 10.1193/062913EQS175M.

Castro-Cruz, D., F. Gatti, F. Lopez-Cabellero, F. Hollender, E. El Haber, and M. Causse (2022). Blind broad-band (0-10 Hz) numerical prediction of the 3-D near field seismic response of an M_w 6.0 extended fault scenario: Application to the nuclear site of Cadarache (France), *Geophys. J. Int.* **232,** no. 1, 581–600, doi: 10.1093/gji/ggac346.

Celebi, M. (1987). Topographical and geological amplifications determined from strong-motion and aftershock records of the 3 March 1985 Chile earthquake, *Bull. Seismol. Soc. Am.* **77,** no. 4, 1147–1167.

Chiou, B. S. J., and R. R. Youngs (2014). Update of the Chiou and Youngs NGA model for the average horizontal component of peak ground motion and response spectra, *Earthq. Spectra* **30,** no. 3, 1117–1153, doi: 10.1193/072813EQS219M.

Cochran, E. S., Y. Li, P. M. Shearer, S. Barbot, Y. Fialko, and J. E. Vidale (2009). Seismic and geodetic evidence for extensive, long-lived fault damage zones, *Geology* **37,** no. 4, 315–318, doi: 10.1130/G25306A.1.

Davis, L. L., and L. R. West (1973). Observed effects of topography on ground motion, *Bull. Seismol. Soc. Am.* **63,** no. 1, 747–763.

De Martin, F., E. C. Chaljub, P. Thierry, P. Sochala, F. Dupros, E. Maufroy, B. Hadri, A. Benaichouche, and F. Hollender (2021). Influential parameters on 3-D synthetic ground motions in a sedimentary basin derived from global sensitivity analysis, *Geophys. J. Int.* **227,** no. 3, 1795–1817, doi: 10.1093/gji/ggab304.

Falgout, J. T., J. Gordon, B. Williams, and M. J. Davis (2019). USGS advanced research computing, USGS Denali supercomputer, *U.S. Geol. Surv.*, doi: 10.5066/P9PSW367.

Frankel, A. D., D. Carver, E. Cranswick, M. Meremonte, T. Bice, and D. Overturf (1999). Site response for Seattle and source parameters of earthquakes in the Puget Sound region, *Bull. Seismol. Soc. Am.* **89,** 468–483.

Frankel, A. D., D. L. Carver, and R. A. Williams (2002). Nonlinear and linear site response and basin effects in Seattle for the M 6.8 Nisqually, Washington, earthquake, *Bull. Seismol. Soc. Am.* **92,** no. 6, 2090–2109, doi: 10.1785/0120010254.

Frankel, A. D., W. J. Stephenson, and D. L. Carver (2009). Sedimentary basin effects in Seattle, Washington: Ground-motion observations and 3D simulations, *Bull. Seismol. Soc. Am.* **99,** no. 3, 1579–1611, doi: 10.1785/0120080203.

Frankel, A. D., W. J. Stephenson, D. L. Carver, R. A. Williams, J. K. Odum, and S. Rhea (2007). Seismic hazard maps for Seattle, Washington, incorporating 3D sedimentary basin effects, nonlinear site response, and rupture directivity, *U.S. Geol. Surv. Open-File Rept. 2007-1175*, 77.

Frankel, A. D., P. Thorne, and A. Rohay (2014). Three-dimensional ground-motion simulations of earthquakes for the Hanford Area, Washington, *U.S. Geol. Surv. Open-File Rept. 2013-1289*, 48, doi: 10.3133/ofr20131289.

Frankel, A. D., E. A. Wirth, N. Marafi, J. Vidale, and W. J. Stephenson (2018). Broadband synthetic seismograms for magnitude 9 earthquakes on the Cascadia megathrust based on 3D simulations and stochastic synthetics, Part 1: Methodology and overall results, *Bull. Seismol. Soc. Am.* **108,** no. 5, 2347–2369, doi: 10.1785/0120180034.

Geli, L., P.-Y. Bard, and B. Jullien (1988). The effect of topography on earthquake ground motion: A review and new results, *Bull. Seismol. Soc. Am.* **78,** no. 1, 42–63.

Graves, R., and A. Pitarka (2016). Kinematic ground-motion simulations on rough faults including effects of 3D stochastic velocity perturbations, *Bull. Seismol. Soc. Am.* **106,** no. 5, 2136–2153, doi: 10.1785/0120160088.

Hartzell, S., D. Carver, E. Cranswick, and A. D. Frankel (2000). Variability of site response in Seattle, Washington, *Bull. Seismol. Soc. Am.* **90,** 1237–1250, doi: 10.1785/0120000022.

Hartzell, S., S. Harmsen, and A. D. Frankel (2010). Effects of 3D random correlated velocity perturbations on predicted ground motions, *Bull. Seismol. Soc. Am.* **100,** no. 4, 1415–1426, doi: 10.1785/0120090060.

Hartzell, S., M. Meremonte, L. Ramírez-Guzmán, and D. McNamara (2014). Ground motion in the presence of complex topography: Earthquake and ambient noise sources, *Bull. Seismol. Soc. Am.* **104,** no. 1, 451–466, doi: 10.1785/0120130088.

Hartzell, S. H., D. L. Carver, and K. W. King (1994). Initial investigation of site and topographic effects at Robinwood Ridge, California, *Bull. Seismol. Soc. Am.* **84,** no. 5, 1336–1349.

Downloaded from http://pubs.geoscienceworld.org/ssa/bssa/article-pdf/113/6/2519/6037178/bssa-2023083.1.pdf
by University of Washington user

Heath, D., D. J. Wald, C. B. Worden, E. M. Thompson, and G. Scmocyk (2020). A global hybrid VS30 map with a topographic-slope-based default and regional map insets, *Earthq. Spectra* **36,** no. 3, 1570–1584, doi: 10.1177/8755293020911137.

Hough, S. E., J. R. Altidor, D. Anglade, D. Given, M. G. Janvier, J. Z. Maharrey, M. Meremonte, B. S. L. Mildor, C. Prepetit, and A. Yong (2010). Localized damage caused by topographic amplification during the 2010 M7.0 Haiti earthquake, *Nature Geosci.* **3,** no. 11, 778–782, doi: 10.1038/ngeo988.

Hu, Z., K. B. Olsen, and S. M. Day (2022). 0-5 Hz deterministic 3-D ground motion simulations for the 2014 La Habra, California, earthquake, *Geophys. J. Int.* **230,** no. 3. 2162–2182, doi: 10.1093/gji/ggac174.

Johnson, S. Y., R. J. Blakely, W. J. Stephenson, S. V. Dadisman, and M. A. Fisher (2004). Active shortening of the Cascadia forearc and implications for seismic hazards of the Puget Lowland, *Tectonics* **23,** TC1011, doi: 10.1029/2003TC001507.

Johnson, S. Y., S. V. Dadisman, J. R. Childs, and W. D. Stanley (1999). Active tectonics of the Seattle fault and central Puget Sound, Washington—Implications for earthquake hazards, *Geol. Soc. Am. Bull.* **111,** no. 7, 1042–1053.

Johnson, S. Y., C. J. Potter, and J. M. Armentrout (1994). Origin and evolution of the Seattle fault and Seattle basin, Washington, *Geology* **22,** no. 1, 71–74.

Komatitsch, D., Q. Liu, J. Tromp, P. Süss, C. Stidham, and J. H. Shaw (2004). Simulations of ground motion in the Los Angeles basin based upon the spectral-element method, *Bull. Seismol. Soc. Am.* **94,** no. 1, 187–206, doi: 10.1785/0120030077.

Lehmann, F., F. Gatti, M. Bertin, and D. Clouteau (2022). Machine learning opportunities to conduct high-fidelity earthquake simulations in multi-scale heterogeneous geology, *Front. Earth. Sci.* **10,** 1–17, doi: 10.3389/feart.2022.1029160.

Lewis, M. A., and Y. Ben-Zion (2010). Diversity of fault one damage and trapping structures in the Parkfield section of the San Andreas fault from comprehensive analysis of near fault seismograms, *Geophys. J. Int.* **183,** 1579–1595, doi: 10.1111/j.1365-246X.2010.04816.x.

Li, Y., J. E. Vidale, and E. S. Cochran (2004). Low-velocity damaged structure of the San Andreas fault at Parkfield from fault zone trapped waves, *Geophys. Res. Lett.* **31,** L12S06, doi: 10.1029/2003GL019044.

Li, Y., J. E. Vidale, D. D. Oglesby, S. M. Day, and E. Cochran (2003). Multiple-fault rupture of the M7.1 Hector Mine, California, earthquake from fault zone trapped waves, *J. Geophys. Res.* **108,** no. B3, ESE11-1–ESE11-25.

Mai, P. M., and G. C. Beroza (2002). A spatial random field model to characterize complexity in earthquake slip, *J. Geophys. Res.* **107,** no. B11, ESE 10-1–ESE 10-21, doi: 10.1029/2001jb000588.

Moschetti, M. P., M. H. Ritzwoller, and N. M. Shapiro (2007). Surface wave tomography of the western United States from ambient noise—Rayleigh wave group velocity maps, *Geochem. Geophys. Geosys.* **8,** no. 8, Q08010, doi: 10.1029/2007GC001655.

National Aeronautics and Space Administration (NASA) Shuttle Radar Topography Mission (SRTM) (2013). Shuttle radar topography mission (SRTM) global, Distributed by OpenTopography, doi: 10.5069/G9445JDF.

National Oceanic and Atmospheric Administration (NOAA) National Centers for Environmental Information (2014). Puget Sound 1/3 arc-second NAVD 88 coastal digital elevation model, available at https://www.ncei.noaa.gov/access/metadata/landing-page/bin/iso?id=gov.noaa.ngdc.mgg.dem:5165 (last accessed April 2021).

Paolucci, R. (2002). Amplification of earthquake ground motion by steep topographic irregularities, *Earthq. Eng. Struct. Dynam.* **31,** no. 10, 1831–1853, doi: 10.1002/eqe.192.

Pedersen, H., B. Le Brun, D. Hatzfeld, M. Campillo, and P. Y. Bard (1994). Ground-motion amplitude across ridges, *Bull. Seismol. Soc. Am.* **84,** no. 6, 1786–1800.

Pischiutta, M., G. Cultrera, A. Caserta, L. Luzi, and A. Rovelli (2010). Topographic effects on the hill of Nocera Umbra, central Italy, *Geophys. J. Int.* **182,** no. 2, 977–987.

Pratt, T. L., S. Y. Johnson, C. Potter, W. J. Stephenson, and C. Finn (1997). Seismic reflection images beneath Puget Sound, western Washington State: The Puget Lowland thrust sheet hypothesis, *J. Geophys. Res.* **102,** no. B12, 27,469–27,489, doi: 10.1029/97JB01830.

Ramachandran, K., R. D. Hyndman, and T. M. Brocher (2006). Regional P wave velocity structure of the Northern Cascadia subduction zone, *J. Geophys. Res.* **111,** no. 12, 1–15, doi: 10.1029/2005JB004108.

Rekoske, J. M., M. P. Moschetti, and E. M. Thompson (2021). Basin and site effects in the U.S. Pacific northwest from small-magnitude earthquakes, *Bull. Seismol. Soc. Am.* **112,** 438–456, doi: 10.1785/0120210029.

Rodgers, A. J., A. Pitarka, R. Pankajakshan, B. Sjögreen, and N. A. Petersson (2020). Regional-scale ground-motion simulations of Mw7 earthquakes on the Hayward fault, northern California resolving frequencies 0-10 Hz and including site-response corrections, *Bull. Seismol. Soc. Am.* **110,** no. 6, 2862–2881, doi: 10.1785/0120200147.

Scalise, M., A. Pitarka, J. N. Louie, and K. D. Smith (2021). Effect of random 3D correlated velocity perturbations on numerical modeling of ground motion from the source physics experiment, *Bull. Seismol. Soc. Am.* **111,** no. 1, 139–156, doi: 10.1785/0120200160.

Sherrod, B. L., T. M. Brocher, and R. C. Bucknam (2002). Asynchronous land-level change along the Tacoma fault in A.D. 800-1200, *Seismol. Res. Lett.* **73,** no. 2, 206, doi: 10.1785/gssrl.73.2.195.

Sherrod, B. L., T. M. Brocher, C. S. Weaver, R. C. Bucknam, H. M. Kelsey, A. R. Nelson, and R. A. Haugerud (2004). Holocene fault scarps near Tacoma, Washington, *Geology* **32,** no. 1, 9–12, doi: 10.1130/G19914.1.

Somerville, P., K. Irikura, R. Graves, S. Sawada, D. Wald, N. Abrahamson, Y. Iwasaki, T. Kagawa, N. Smith, and A. Kowada (1999). Characterizing crustal earthquake slip models for the prediction of strong ground motion, *Seismol. Res. Lett.* **70,** no. 1, 59–80, doi: 10.1785/gssrl.70.1.59.

Spudich, P., M. Hellweg, and W. H. K. Lee (1996). Directional topographic site response at Tarzana observed in aftershocks of the 1994 Northridge, California, earthquake: Implications for mainshock motions, *Bull. Seismol. Soc. Am.* **86,** no. 1B, S193–S208.

Stephenson, W. J., N. G. Reitman, and S. J. Angster (2017). P- and S-wave velocity models incorporating the Cascadia subduction zone for 3D earthquake ground motion simulations—Update for Open-File Report 2007–1348, *U.S. Geol. Surv. Open-File Rept. 2017-1152*, 17 pp., doi: 10.3133/ofr20171152.

Downloaded from http://pubs.geoscienceworld.org/ssa/bssa/article-pdf/113/6/2519/6037178/bssa-2023083.1.pdf
by University of Washington user

Stone, I., E. A. Wirth, and A. D. Frankel (2022). Topographic response to simulated M_w 6.5–7.0 earthquakes on the Seattle fault, *Bull. Seismol. Soc. Am.* **112,** no. 3, 1436–1462, doi: 10.1785/0120210269.

Thompson, M., E. A. Wirth, A. D. Frankel, J. R. Hartog, and J. E. Vidale (2020). Basin amplification effects in the Puget Lowland, Washington, from strong-motion recordings and 3D simulations, *Bull. Seismol. Soc. Am.* **110,** no. 2, 534–555, doi: 10.1785/0120190211.

Wald, D. J., and T. I. Allen (2007). Topographic slope as a proxy for seismic site conditions and amplification, *Bull. Seismol. Soc. Am.* **97,** no. 5, 1379–1395, doi: 10.1785/0120060267.

Wells, D. L., and K. J. Coppersmith (1994). New empirical relationships among magnitude, rupture length, rupture width, rupture area, and surface displacement, *Bull. Seismol. Soc. Am.* **84,** no. 4, 974–1002.

Wirth, E. A., S. W. Chang, and A. D. Frankel (2018). *2018 Report on Incorporating Sedimentary Basin Response into the Design of Tall Buildings in Seattle, Washington, Open-File Rept. 2018-1149*, U.S. Geological Survey, Reston, Virginia, U.S.A., 19, doi: 10.3133/ofr20181149.

Wirth, E. A., A. D. Frankel, N. Marafi, J. E. Vidale, and W. J. Stephenson (2018). Broadband synthetic seismograms for magnitude 9 earthquakes on the Cascadia megathrust based on 3D simulations and stochastic synthetics, Part 2: Rupture parameters and variability, *Bull. Seismol. Soc. Am.* **108,** no. 5, 2370–2388, doi: 10.1785/0120180029.

Wirth, E. A., A. Grant, N. A. Marafi, and A. D. Frankel (2021). Ensemble ShakeMaps for magnitude 9 earthquakes on the Cascadia subduction zone, *Seismol. Res. Lett.* **92,** no. 1, 199–211, doi: 10.1785/0220200240.

Wirth, E. A., J. E. Vidale, A. D. Frankel, T. L. Pratt, N. A. Marafi, M. Thompson, and W. J. Stephenson (2019). Source-dependent amplification of earthquake ground motions in deep sedimentary basins, *Geophys. Res. Lett.* **46,** no. 12, 6443–6450, doi: 10.1029/2019GL082474.

Yang, H., and L. Zhu (2010). Shallow low-velocity zone of the San Jacinto fault from local earthquake waveform modelling, *Geophys. J. Int.* **183,** 421–432, doi: 10.1111/j.1365-246X.2010.04744.x.

Manuscript received 1 May 2023
Published online 6 September 2023

Downloaded from http://pubs.geoscienceworld.org/ssa/bssa/article-pdf/113/6/2519/6037178/bssa-2023083.1.pdf
by University of Washington user